

CHAPTER 2

Spaceborne Synthetic Aperture Radar: Principles, Data Access, and Basic Processing Techniques

Franz Meyer, Associate Professor for Radar Remote Sensing, UAF & Chief Scientist of Alaska Satellite Facility

ABSTRACT

This chapter provides background information and hands-on processing exercises on the main concepts of Synthetic Aperture Radar (SAR) remote sensing. After a short introduction on the peculiarities of the SAR image acquisition process, the remainder of this chapter is dedicated to supporting the reader in interpreting the often unfamiliar-looking SAR imagery. It describes how the appearance of a SAR image is influenced by sensor parameters (such as signal polarization and wavelength) as well as environmental factors (such as soil moisture and surface roughness). A comprehensive list of past, current, and planned SAR sensors is included to provide the reader with an overview of available SAR datasets. For each of these sensors, the main imaging properties are described and their most relevant applications listed. An explanation of SAR data types and product levels with their main uses and information on means of data access concludes the narrative part of this chapter and serves as a lead-in to a set of hands-on data processing techniques. These techniques use public domain software tools to walk the reader through some of the most relevant SAR image processing routines, including geocoding and radiometric terrain correction, interferometric SAR processing, and change detection.

2.1 On the Concepts of Imaging Radars

2.1.1 A WORD ABOUT HISTORY

The invention of RAdio Detection And Ranging, or radar, as a concept for detecting and localizing objects in a three-dimensional space dates back to the turn of the 20th century and is typically credited either to the German inventor and entrepreneur Christian Huelsmeyer—who proposed the so-called “Telemobiloskop” as an active microwave-based system for detecting distant metallic objects (Vollmar 1960)—or to the British engineer Robert Watson-Watt, who in June of 1935 successfully demonstrated an object detection and ranging system that was capable of accurately locating airborne objects up to a distance of about 30 km (Watson-Watt 1946). Once invented, radar technology developed rapidly during the World War II era, motivated mostly by air defense and over-the-horizon surveillance considerations. By the early 1940s, radars had become small enough to be implemented on airplanes, expanding the application

realm of radar systems into a range of new fields, including the growing discipline of Earth observation. This chapter discusses the application of imaging radar sensors to this discipline.

2.1.2 SIDE-LOOKING AIRBORNE RADARS

The allure of using radar systems for imaging purposes mostly stems from the all-weather and all-day capabilities that can be provided by this sensor type. These capabilities are advantageous for many surveillance applications, allowing for regular mapping of areas affected by heavy cloud cover, persistent rain, or extended darkness. Additionally, radar signals interact differently with the surface than most other sensing systems, providing interesting new information about the observed environment.

With the development of Side-Looking Airborne Radar (SLAR) systems in the 1950s, the first airborne radar systems with reliable imaging performance became available. The observation configuration of a SLAR system is shown in **Figure 2.1** and consists of a radar sensor mounted on an airborne (or spaceborne) platform that, in this simplified exam-

ple, is moving along a straight path at altitude H . Unlike most optical imaging systems, which point their sensors towards nadir, the antenna of a SLAR (and any other imaging radar) system is pointed away from nadir by a so-called look angle θ , such that it illuminates a continuous swath on the ground as the aircraft moves along.

While flying along its track, the radar system is transmitting a sequence of short microwave pulses of pulse length τ_p , each of which illuminates an instantaneous area on the ground that is usually referred to as the antenna footprint (see darker gray area in **Fig. 2.1**). The size S of this instantaneous footprint in either the range or along-track (azimuth) direction is largely defined by the relationship between system wavelength λ and the side length of the antenna L (defining the antenna’s beamwidth through $\beta = \lambda/L$) along this direction, as well as by the distance of the radar sensor from the ground R :

$$S \approx \frac{\lambda}{L} R = \beta \cdot R \text{ [m]} . \quad (2.1)$$

To form a two-dimensional image, the echoes received from the ground are sorted by their arrival

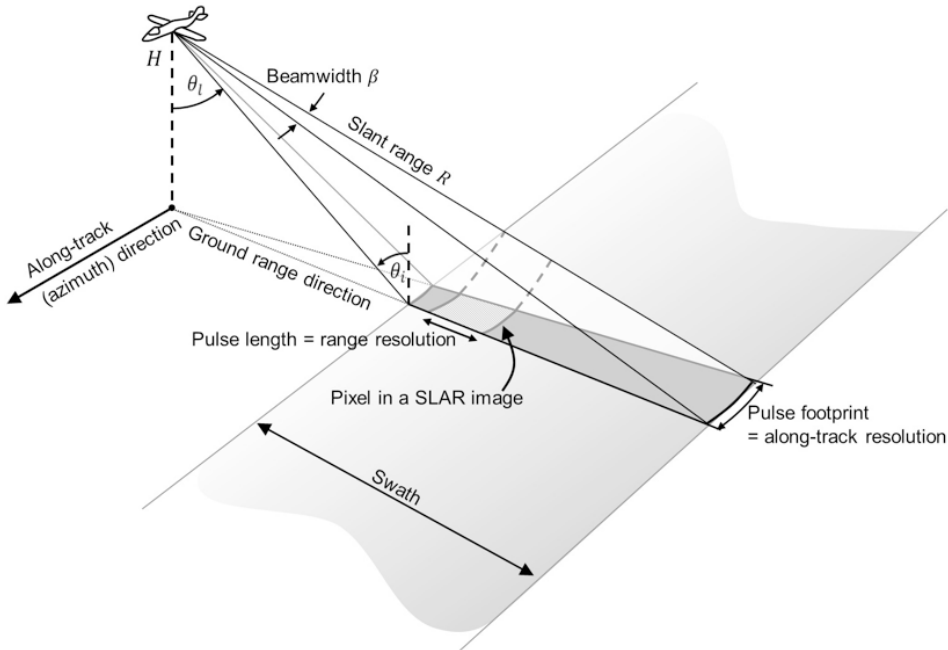


Figure 2.1 Observation geometry of a SLAR imager. The radar flies along a straight line at altitude H and observes Earth at an oblique look angle θ_l . Instead of the look angle, sometimes the incidence angle $\theta_i = (90^\circ - \theta_l)$ is annotated. The size of the illuminated footprint is defined by the antenna beamwidth β and the distance between satellite and ground R . Note that the radar beam is wide in range direction but narrow in azimuth. The generation of an image is facilitated by the forward motion of the airborne platform.

time in both range and azimuth direction. In range direction, echoes from the ground arrive progressively later from the near-range to the far-range edge of the swath. Objects at different ranges can be distinguished if their range separation is larger than half the transmitted pulse length. Hence, the range resolution of a SLAR system is defined by

$$\rho_R = \frac{c \cdot \tau}{2} \text{ [m]}, \quad (2.2)$$

with c corresponding to the speed of light. The variable ρ_R in Eq. (2.2) is usually referred to as the slant range resolution of a SLAR system as it describes a SLAR's ability to distinguish objects at different (slant) distances from the radar (see "slant range direction" in Fig. 2.1). While the slant range parameter ρ_R is useful for many system design questions, remote sensing is often more interested in the ground range resolution ρ_G , which describes the ability to discriminate objects that are situated on the ground and is calculated from ρ_R via the local incidence angle θ_i :

$$\rho_G = \frac{\rho_R}{\sin(\theta_i)} \text{ [m]}. \quad (2.3)$$

Eq. (2.3) shows that the ground range resolution

ρ_G is not constant across the swath and actually improves with distance from nadir (due to the increase of θ_i). This is opposite to the behavior of most optical systems for which the ground resolution degrades with increasing θ_i .

In the along-track (or azimuth) direction, the ground is scanned by the movement of the radar along its track. In the case of SLAR systems, the azimuth resolution ρ_{Az} (the ability to discriminate objects in azimuth direction) is defined by the width of the antenna footprint in azimuth S_{Az} which, in turn, is limited by the side length L_{Az} of the antenna in this direction. Hence, following Eq. (2.1), the azimuth resolution corresponds to

$$\rho_{Az} = S_{Az} \approx \frac{\lambda}{L_{Az}} R = \beta_{Az} \cdot R \text{ [m]}. \quad (2.4)$$

Eq. (2.4) indicates that the azimuth resolution ρ_{Az} is linearly degrading with increasing distance between the sensor and the ground R . This has two important implications for SLAR systems: first, as R changes from the near-range to the far-range edge of the swath, the azimuth resolution of a SLAR is not

constant across range. Second, and more importantly, the dependence of ρ_{Az} on the distance to the ground R makes the application of SLAR systems on high-altitude or even spaceborne platforms highly impractical. To illustrate this point, assume a C-band SLAR system operating at $\lambda = 0.03$ [m] and utilizing an antenna of $L = 3$ [m] length. If operated from an aircraft at $H = 3000$ [m] altitude and observing at a look angle of $\theta_l = 30^\circ$, this system will achieve an acceptable azimuth resolution of $\rho_{Az} = 0.01 \cdot 3000 \cdot 2 = 60$ [m]. However, if the same system is operated from a spaceborne platform at $H = 800$ [km], ρ_{Az} will degrade to $\rho_{Az} = 16$ [km], which is below the required system performance for most Earth observation applications.

A straightforward approach for keeping the system's azimuth resolution at an acceptable level even for spaceborne applications is to increase the length of the antenna used by the system until a desired value for ρ_{Az} is reached. Simple mathematics show, however, that this solution is not practical. Using the numbers from the previous example we find that an unreasonable antenna length of about $L = 800$ [m] would be needed to achieve a $\rho_{Az} = 60$ [m] resolution from space. An elegant and more practical solution for the azimuth resolution issue—the synthetic aperture principle—was developed in 1952 and will be introduced in Section 2.1.3.

Despite their resolution limitations, SLAR systems remain popular for many ground-based and airborne applications. This continued popularity is largely due to the simplicity of SLAR systems in both their system design and data processing demands.

2.1.3 SYNTHETIC APERTURE RADAR SENSORS

In 1952, Carl Wiley, an engineer with the Good-year Aircraft Cooperation, made an essential discovery that provided a solution to the azimuth resolution problem plaguing existing SLAR technology (see Sec. 2.1.2). In technical terms, he observed that a one-to-one correspondence exists between the along-track coordinate (relative to a transmitted radar beam) of a reflecting object and the instantaneous Doppler shift of the signal reflected back to the radar by that object. He further postulated that a frequency analysis of the recorded signals could en-

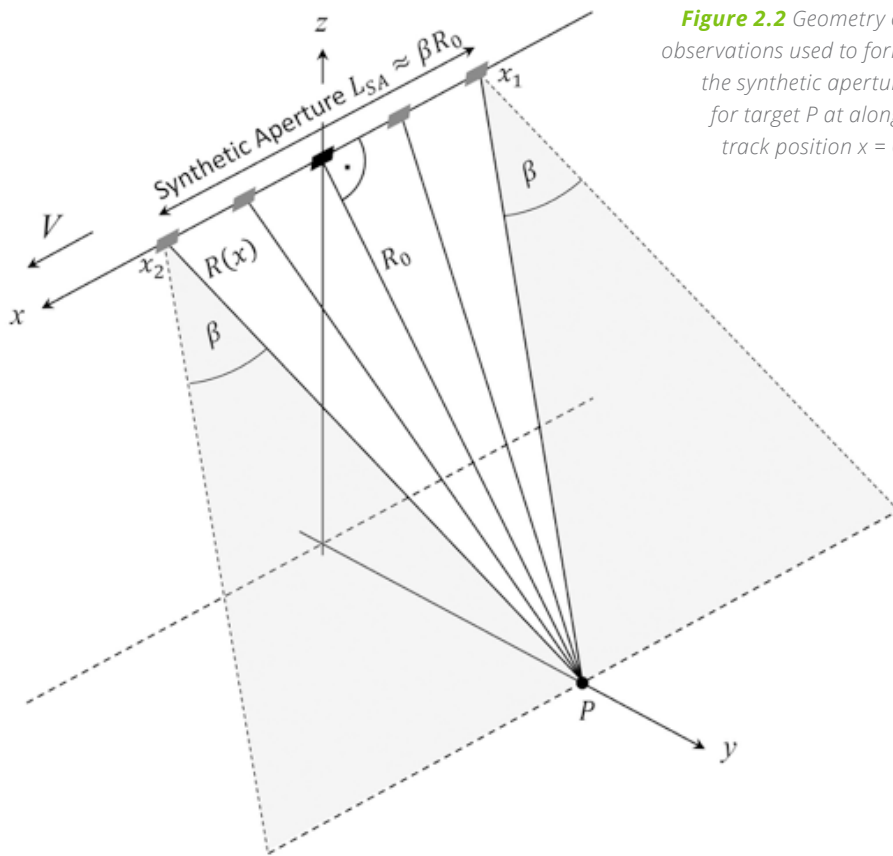


Figure 2.2 Geometry of observations used to form the synthetic aperture for target P at along-track position $x = 0$.

able a finer along-track resolution than that achieved by conventional SLAR systems. Wiley's discovery—which was originally published under the name Doppler beam-sharpening but is often referred to as aperture synthesis—is the key element behind all modern high-resolution imaging radar systems. There is a large body of literature on the mathematical details of Wiley's aperture synthesis solution to radar imaging. Readers interested in more technical information should refer to the excellent summary by Cumming and Wong (2005).

The following conceptual explanations of Wiley's invention provide a good summary. The aperture synthesis principle essentially allows one to create (or "synthesize") a much longer effective antenna (the so-called synthetic aperture) from a sequence of acquisitions made with a shorter antenna as it moves along its flight line. As antenna length is intrinsically linked to the resolution capabilities of a radar system (we know this from Eq. (2.1)), the much longer antenna synthesized by Wiley's principle allows high-resolution imaging even from spaceborne platforms using

antenna hardware of a manageable size.

A simplified conceptual illustration of Wiley's concept is shown in **Figure 2.2**. There, a radar antenna (indicated by a gray rectangle) of reasonably short length is moving at a velocity V along its flight path from the right to the left. While moving, it is constantly transmitting short radar pulses and receiving echoes returned from objects on the ground. Each radar pulse illuminates an instantaneous footprint of size S on the Earth surface. For spaceborne applications, the limited length L of the radar antenna (Eq. (2.1)) results in instantaneous footprints that typically measure several kilometers in size, resulting in the typical resolution limitation that plagues SLAR systems.

To apply Wiley's aperture synthesis concept, we have to first ensure that an object P on the Earth surface is imaged by many consecutive radar pulses as the antenna beam sweeps across the ground. This requirement is indicated in **Figure 2.2** by several antenna positions that illuminate object P as the sensor moves from point x_1 (first time object P is seen) to

point x_2 (last time P is observed). Once the radar data are acquired, a postprocessing approach is applied to combine all acquisitions between x_1 and x_2 and into a single dataset that looks like it was acquired with a much longer antenna. This longer (virtual) antenna is typically called the "synthetic aperture," as it was synthesized from a number of acquisitions with shorter antennas. The length L_{SA} of this synthetic aperture can be calculated via

$$L_{SA} = \frac{\lambda}{L} \cdot R_0 \approx \beta \cdot R_0$$

and is equivalent to the footprint S illuminated by the (shorter) real antenna installed on the spacecraft (see Eq. (2.1)).

The dataset resulting from the aperture synthesis process is typically referred to as a SAR image and has much higher resolution than SLAR images acquired from the same distance. An example of a SAR image acquired by the European Space Agency's (ESA's) ERS-2 sensor is shown in **Figure 2.3**.

The aperture synthesis concept is the basis of all modern radar systems even though various modifications of the basic imaging concept are currently used to maximize either image resolution (Spotlight concept: Eineder et al. 2009, Lanari et al. 2001, Mittermayer et al. 1999) or image coverage (ScanSAR: Bamler and Eineder 1996, Bamler and Holzner 2004, Monti Guarnieri and Prati 1996). Modern spaceborne SAR sensors typically achieve ground resolutions between roughly 0.5 and 20 m, depending on their specific design. Recent developments in antenna design and image processing

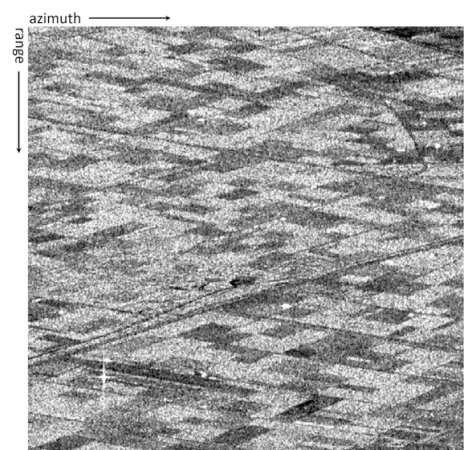


Figure 2.3 Example of a spaceborne SAR dataset acquired by ESA's C-band sensor ERS-2.

techniques have made high-resolution imaging across large image swaths possible. These developments rely on the concept of digital beamforming (Gebert et al. 2009, Krieger & Moreira 2003, Younis et al. 2003) and have spawned new imaging modes such as Terrain Observation with Progressive Scans SAR (TOPSAR) (De Zan & Monti Guarnieri 2006) and SweepSAR (Freeman et al. 2009). For technical details on these techniques, please see the literature cited.

2.1.4 GEOMETRIC PROPERTIES OF SAR DATA

Due to the oblique observation geometry inherent to all imaging radar systems, surface slopes and similar terrain features lead to geometric distortions in data acquired by SAR systems. The most relevant of these distortions are foreshortening, layover, and shadow. The origins and main characteristics are of these distortions are summarized in **Figure 2.4**.

In side-looking viewing geometries, sensor-facing slopes appear foreshortened such that a symmetric mountain would appear in the radar image as if “leaning” towards the sensor. The geometric background of foreshortening is shown in **Figure 2.4(a)**, showing that the slope between points *A* and *B* will get foreshortened into the image area *A'B'*. The amount of foreshortening depends both on the system’s look angle θ and on the slope angle α , and reaches its maximum if $\theta \rightarrow \alpha$. In areas where $\theta < \alpha$ (e.g., in areas of steep slopes combined with steep incidence angles), foreshortening turns into layover (see **Fig. 2.4(b)**). In layover situations, the tops of mountains are imaged ahead of their base (see projections of points *B* and *C* in **Fig. 2.4(b)**) and backscatter from mountain slopes will overlay with image information at closer and farther image ranges (see green, red, and gray areas in **Fig. 2.4(b)**). Both foreshortening and layover can be reduced if the look angle θ is increased; however, larger θ will produce more image shadow (**Fig. 2.4(c)**). Hence, topography-related image distortions cannot be entirely removed, and image acquisitions from more than one vantage point may be necessary to jointly minimize all three imaging effects.

2.1.5 RADIOMETRIC PROPERTIES – THE SPECKLE EFFECT

Besides these geometric distortions, SAR images additionally are characterized by a somewhat grainy

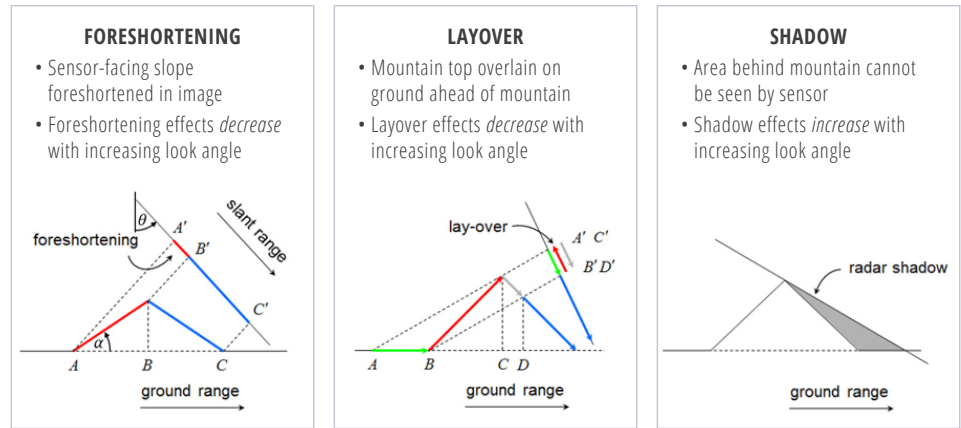


Figure 2.4 Main geometric distortions on SAR images with their dependence on acquisition geometry: (a) foreshortening, (b) layover, and (c) shadow.

appearance that resembles “salt and pepper” noise. This noise-like pattern can be seen in **Figure 2.3** and is usually referred to as “speckle.” The speckle effect is inherent to all narrow-banded coherent imaging systems and is a result of interference from the many scattering echoes within a resolution cell.

In a medium-resolution SAR image, the scattering response from one resolution cell (of about 10×10 [m] in size) is the coherent sum of thousands of individual scattering events, as shown in **Figure 2.5(a)**. Imagine the SAR system is imaging a homogeneous surface, such as a smooth meadow, and assume that the individual scattering events within one resolution cell (gray arrows in **Fig. 2.5(a)**) are all about equally strong. Due to their different positions within the resolution cell, the phase of the individual scatterers will vary randomly, such that the scattering response from one pixel is the summation of thousands of random vectors (black arrow in **Fig. 2.5(a)**). As the arrangement of scatterers in different resolution cells is not identical even for homogeneous targets, both the amplitude and phase of the summation vector (black arrow) will vary randomly from pixel to pixel, resulting in the typical grainy signature shown previously in **Figure 2.3**. If the number of individual scattering events is large, the distribution of intensities in a SAR image follows an exponential distribution of the form

$$pdf(I|\sigma^0) = \frac{1}{\sigma^0} \exp\left\{-\frac{I}{\sigma^0}\right\}, \quad (2.5)$$

where $I = Re\{u\}^2 + Im\{u\}^2$ is the image intensity in

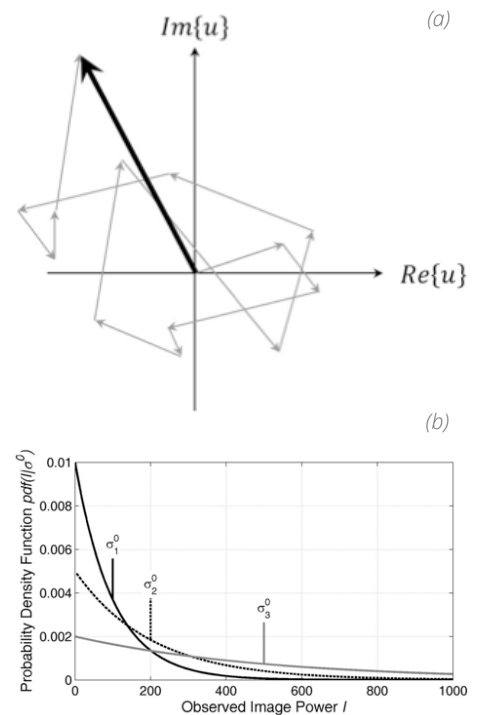


Figure 2.5 (a) Speckle originating from the coherent summation of many individual scattering events within a resolution cell and (b) shape of the speckle pdf for images areas with different normalized radar cross sections σ^0 .

a pixel. The distribution in Eq. (2.5) is often called speckle distribution and is a valid description for the noise patterns observed for homogeneous targets in medium-resolution SAR images.

Eq. (2.5) shows that the shape of the speckle distribution depends on the (true) normalized radar cross section σ^0 of the observed target, such that

brighter image patches will show more intense noise. Here, σ^0 describes the percentage of incoming radar energy that is scattered back to the sensor by an object on the ground. It is a normalized version of Eq. (2.6) discussed in the next section. The dependence of the speckle statistics on σ^0 is visualized in **Figure 2.5(b)**, where the speckle distribution $\text{pdf}(I|\sigma^0)$ is plotted for three different σ^0 values. It can be seen that the speckle distribution becomes wider with increasing σ^0 and starts to approximate a uniform distribution for very high σ^0 .

Speckle noise is distinguished from most other noise sources, which are often constant throughout the image, by its dependence on image brightness. Multiplicative noise such as speckle is difficult to treat, as the true radar cross section σ^0 of the target needs to be known to correctly model $\text{pdf}(I|\sigma^0)$. Hence, throughout the last decade, a lot of effort has been dedicated to the development of effective speckle filters, resulting in a wealth of different filtering methods. While the most relevant/well known of these filters are listed in **Table 2.1**, readers interested in this topic are referred to specialized literature such as Bruniquel & Lopes 1997, Ferretti et al. 2011, Huang et al. 2009, Lee et al. 1991, Lee et al. 1994, Lopez-Martinez & Pottier 2007, Novak & Burl 1990, and Sveinsson & Benediktsson 2003.

2.2 How SAR Images the World

SARs transmit microwave signals at an oblique angle and measure the backscattered (in the direction of the sensor) portion of this signal in order to analyze features on the surface. Mathematically, this (calibrated) measurement is described using the term Radar Cross Section (RCS) σ , which is defined as the ratio between the incident and received signal intensity:

$$\sigma = \frac{I_{\text{received}}}{I_{\text{incident}}} 4\pi R^2 \left[m^2 \right]. \quad (2.6)$$

The RCS recorded by a SAR for a specific surface feature is not always straightforward to interpret, as it is influenced both by a range of scene characteristics as well as by the parameters of the imaging sensor.

The most important scene parameters driving RCS are surface roughness h_{rough} and the dielectric properties of the imaged object quantified by its complex relative dielectric constant ϵ_r . While h_{rough} describes how much of the scattered radar energy is directed back to the sensor, the dielectric properties guide

whether or not (and how deep) signals may penetrate into the scattering surface. The fact that both of these parameters are a function of sensor wavelength (and to some degree signal polarization) explains why the characteristics of the sensor play a role when attempting to interpret the measured signature of real-life objects in a SAR image.

2.2.1 DIELECTRIC PROPERTIES AND PENETRATION DEPTH OF RADAR SIGNALS

The dielectric properties of a medium govern how a microwave signal of wavelength λ interacts with a scattering medium such as the Earth's surface or a vegetation canopy. These properties dictate how much of the incoming radiation scatters at the surface, how much signal penetrates into the medium, and how much of the energy gets lost to the medium through absorption. While a detailed explanation of microwave scattering processes is beyond the scope of this chapter, information is provided on how these processes change with sensor wavelength. This will provide the reader with the required background to interpret differences in the appearance of observed data from different SAR instruments. For a more detailed discussion on the interactions of microwaves with media, please refer to the excellent introducto-

SPECKLE FILTERS	DESCRIPTION	RELATED PUBLICATION(S)
Change-preserving multi-temporal Speckle filter	Filter for stacks of SAR images; reduces speckle while preserving changes in the time series (e.g., related to deforestation)	Quegan and Yu, 2001
Lee filter	Standard deviation-based (sigma) filter, filtering data based on statistics calculated from the data. Unlike a Gaussian or boxcar filter, the Lee filter and other similar sigma filters preserve image sharpness and detail while suppressing noise.	Lee, 1980
Enhanced Lee filter	The enhanced Lee filter is an adaptation of the Lee filter. Each pixel is put into one of three classes, which are treated as follows: <u>Homogeneous</u> : The pixel value is replaced by the average of the filter window. <u>Heterogeneous</u> : The pixel value is replaced by a weighted average. <u>Point target</u> : The pixel value is not changed.	Lopes et al., 1990
Frost and enhanced Frost filters	The Frost filter is an exponentially damped circularly symmetric filter that uses local statistics. The Enhanced Frost filter is an adaptation of the Frost filter. It classifies and filters pixels according to the logic explained in the row above.	Frost et al., 1982; Lopes et al., 1990
Non-local means filters	The basic idea behind non-local means filters is to provide an estimate of the clean image via a proper averaging of similar pixels or patches, found in the image. Essentially, the algorithm searches for image patches that resemble the area around the pixel to be filtered. Using some similarity criterion, these patches are found and averaged together to de-noise the image without losing resolution.	Buades et al., 2005; Chen et al., 2014; Di Martino et al., 2016; Martino et al., 2015

Table 2.1 Summary of most relevant speckle filters with their properties and related publications.

ry book on microwave remote sensing by Iain Woodhouse (2006).

Figure 2.6 provides a conceptual overview of the influence of sensor wavelength λ on signal penetration into a variety of surface types. The radar signals penetrate deeper as sensor wavelength increases. This is related to the dependence of the dielectric constant ϵ_r on the incident wavelength, allowing for higher penetration at L-band than at C- or X-bands. For vegetated areas, this implies that X-band SAR sensors mostly scatter at the tops of tree canopies, while C- and L-band signals penetrate increasingly deeper into the vegetation volume. Hence, if vegetation parameters (e.g., vegetation structure, biomass, etc.) are to be characterized using SAR, longer wavelength systems should be used (see **Table 2.3** to identify sensors operating at longer wavelengths). Similarly, users interested in mapping inundation under forest canopies should select longer wavelength SAR sensors as their main data source.

In addition to sensor wavelength, the penetration depth of a SAR signal into a vegetation canopy is also influenced by the density of this canopy. For example, while C-band SAR data may “see” the ground underneath sparse boreal forests, C-band signals will not be able to fully penetrate the denser and layered canopy structure of rainforests.

The rule of increasing penetration with increasing sensor wavelength also holds true for bare surfaces such as alluvium soils or glacier ice; X-band signals scatter close to the surface, while C- and L-band data penetrate progressively deeper into the medium. To quantify penetration depths δ_p into bare surfaces, information about the dielectric properties ϵ_r of the medium is needed. If information on ϵ_r is available, δ_p can be approximated by

$$\delta_p \approx \lambda \sqrt{\epsilon_r'} / (2\pi \epsilon_r''), \quad (2.7)$$

where ϵ_r' is the real component and ϵ_r'' is the imaginary component of the complex relative dielectric constant. In addition to soil density and sensor wavelength, ϵ_r' and ϵ_r'' are strongly dependent on the moisture content of the medium. **Figure 2.7(a)** shows an example of the dependence of dielectric properties on moisture content for loam soils com-

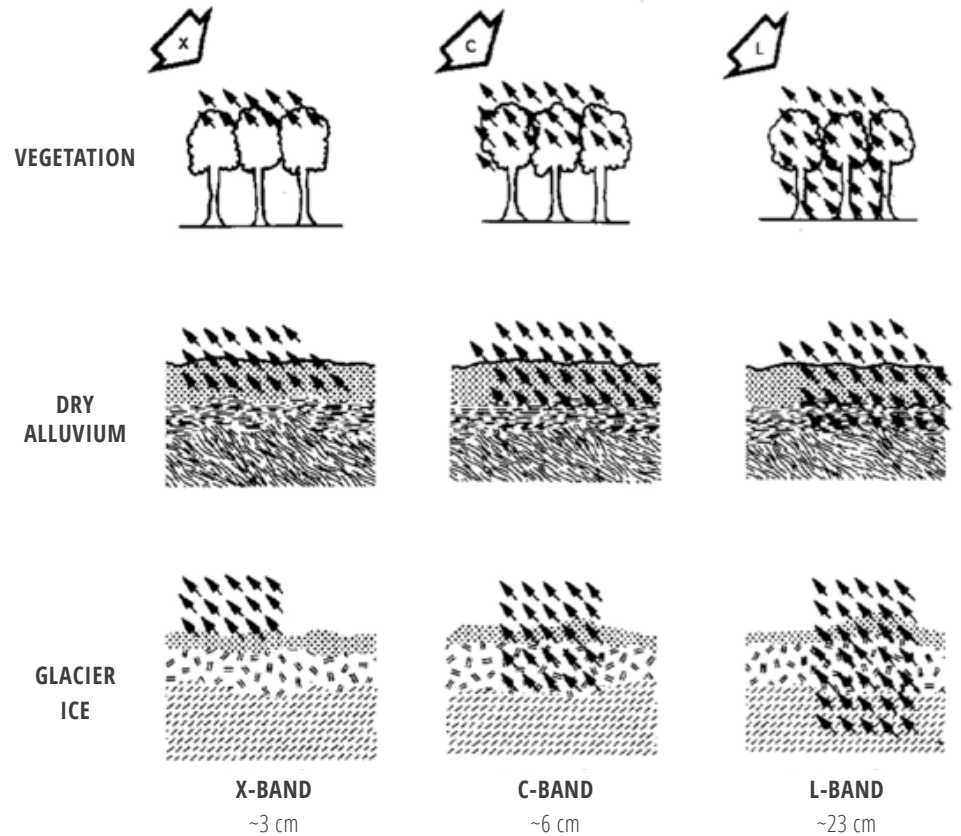


Figure 2.6 SAR signal penetration by sensor wavelength λ .

posed of a mix of sand, silt, and clay ingredients. The dielectric properties are plotted as a function of soil moisture for several sensor wavelengths. It can be seen that both ϵ_r' and ϵ_r'' increase with soil moisture, leading to a reduction of penetration depth according to Eq. (2.7). Also, ϵ_r' and ϵ_r'' depend on sensor frequency $f = c/\lambda$. With increasing frequency (decreasing wavelength), ϵ_r' reduces and ϵ_r'' increases such that penetration depth δ_p is significantly larger for low-frequency (long wavelength) SARs. A plot of the dependence of penetration depth δ_p on sensor wavelength λ is shown in **Figure 2.7(b)**. Penetration depth is approximated according to Eq. (2.7) for the soil type shown in **Figure 2.7(a)** and assuming a volumetric soil moisture of 0.35. A near-linear increase of penetration depth with increasing sensor wavelength can be observed.

2.2.2 SURFACE ROUGHNESS

With few exceptions (dry snow, dry sandy soils), most bare or low-vegetation surfaces allow very little

penetration for microwave radiation (**Fig. 2.7(b)**) such that surface scattering dominates the measured radar response. In these cases, the roughness of the scattering surface is the main driver defining the observed RCS in a SAR scene.

For narrow-band imaging systems like SAR, whether a surface appears rough or not can only be decided with the observing sensor wavelength in mind. If the scale of roughness of a randomly rough surface is characterized using the standard deviation of the height deviation h from some mean height \bar{h} of the surface, then the question of how large h has to be for a surface to appear rough to an observing SAR system can be answered. According to the Fraunhofer criterion, a surface is defined as rough if the height deviations exceed the value h_{rough} , which is determined by Eq. (2.8):

$$h_{\text{rough}} > \lambda / ((32 \cdot \cos\theta)) . \quad (2.8)$$

Note that the relationship in Eq. (2.8) depends on the signal wavelength λ and indicates that a surface with fixed height variations h may qualify as rough in

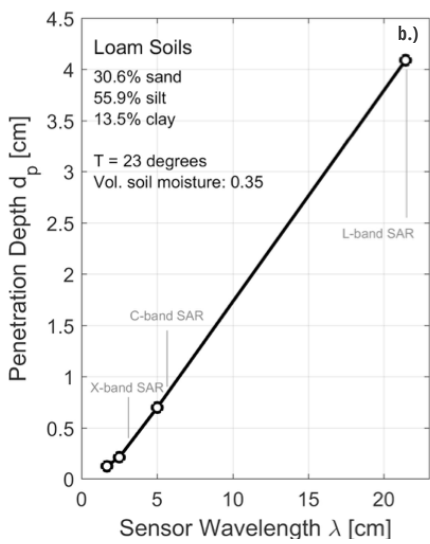
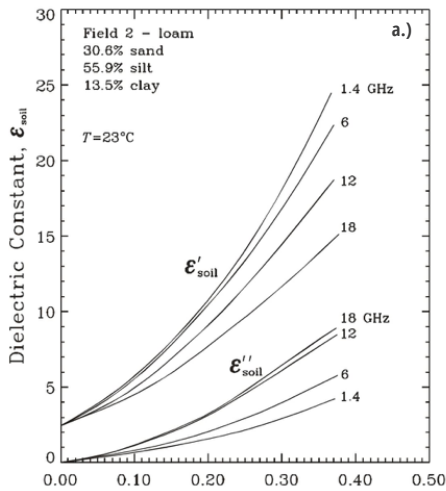


Figure 2.7 (a) Relationship between soil moisture and dielectric constant and (b) dependence of penetration depth δ_p on sensor wavelength λ for a fixed soil moisture.

X-band but possibly not in C- or L-bands. This concept of wavelength-dependent roughness is visualized in **Figure 2.8**, which shows increasing roughness conditions from left to right and identifies the transition from smooth (**Fig. 2.8(a)**) to intermediately rough (**Fig. 2.8(b)**) to rough surfaces (**Fig. 2.8(c)**) in accordance with the Fraunhofer criterion in Eq. (2.8). It can be seen that the amount of backscatter increases (length of blue arrows pointing toward the sensor) as roughness increases such that rough surfaces (at wavelength λ) have higher RCS than intermediately rough or smooth surfaces. The wavelength dependence also means that a surface will look increas-

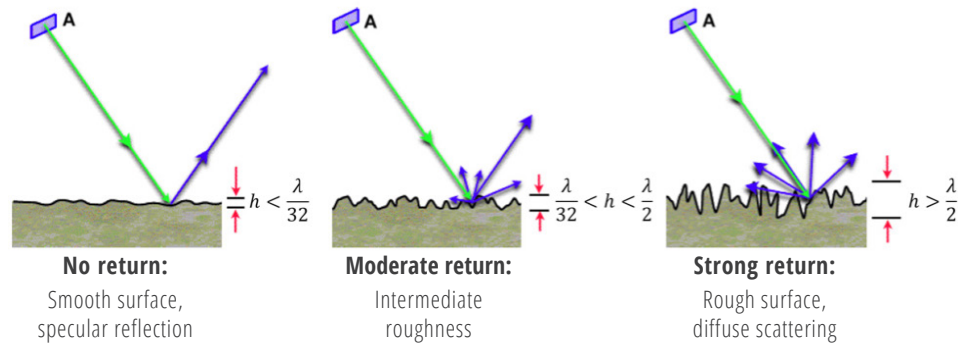


Figure 2.8 Conceptual sketch of the dependence of surface roughness on the sensor wavelength λ : (a) smooth, (b) intermediate, and (c) rough.

ingly darker as wavelength increases from X-band ($\lambda = 3.1$ cm) through C-band ($\lambda = 5.66$ cm) to L-band ($\lambda = 24$ cm).

2.2.3 THE INFLUENCE OF SIGNAL POLARIZATION

As SAR is an active instrument with its own source of illumination, it is one of the few sensing instruments that allows one to fully control (and fully exploit) the polarization of the signal on both the transmit and the receive paths. Polarization describes the orientation of the plane of oscillation of a propagating signal. In linearly polarized systems, the orientation of this plane of oscillation is constant along the propagation path of the electromagnetic wave. In other systems, such as circular or elliptically polarized SARs, the orientation of the oscillation plane changes, describing geometric shapes such as ellipses or circles.

The majority of today's SAR sensors are linearly polarized and transmit horizontally and/or vertically polarized wave forms. Many of the heritage SAR satellites carry single-polarized sensors, which support only one linear polarization. These sensors predominantly operate in HH- (horizontal polarization on transmit; horizontal polarization on receive) or VV-polarization (vertical transmit; vertical receive), while single-polarized sensors transmitting one linear polarization and receiving the other (e.g., HV (horizontal transmit; vertical receive) are rare in practice.

More recent sensors provide either dual-polarization or quad-polarization capabilities. In the latter,

the sensor alternates between transmitting H- and V-polarized waveforms and receiving both H and V simultaneously, providing HH-, HV-, VH-, and VV-polarized imagery.

Knowing the polarization from which a SAR image was acquired is important, as signals at different polarizations interact differently with objects on the ground, affecting the recorded radar brightness in a specific polarization channel. While the details of polarimetric scattering are beyond the scope of this chapter, the following paragraph provides rules of thumb that should aid in the interpretation of polarimetric SAR data.

For simplicity, it is assumed that a natural scene can be described as a combination of three types of scatterers: (1) rough surface scatterers, (2) double-bounce scatterers, and (3) volume scatterers. The nature of these scattering types is illustrated in **Figure 2.9**. The category of surface scatterers (shown in blue in **Fig. 2.9**) is made up of low-vegetation fields and bare soils, as well as roads and other paved surfaces. Double-bounce scatterers (red in **Fig. 2.9**) include buildings, tree trunks, light poles, and other vertical structures that deflect an initial first forward reflection back to the sensor. Finally, vegetation canopies belong to the category of volume scatterers (green in **Fig. 2.9**) as the signals bounce multiple times as they propagate through the vegetation structure.

It turns out that these scattering types do not contribute to all polarimetric channels equally. Instead, each polarimetric channel "prefers" certain scattering types such that the scattering power $|S|$ in the indi-

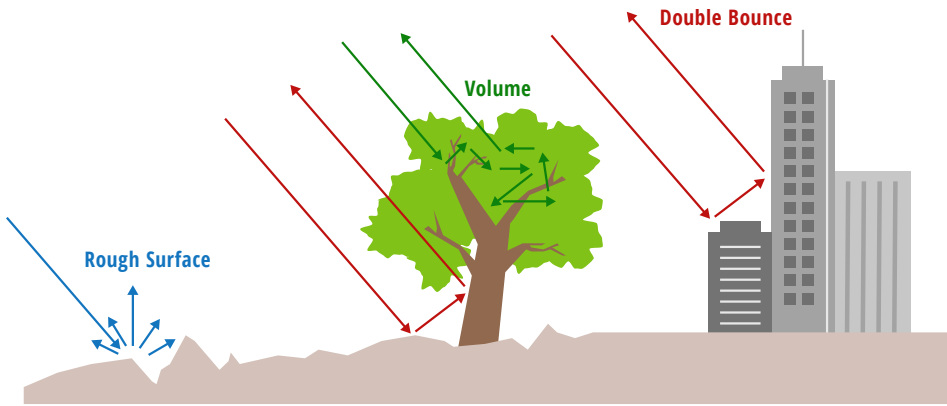


Figure 2.9 Schematic sketch of the three main scattering types considered for SAR data.

vidual polarimetric channels follows the following general scheme shown in Table 2.2.

RELATIVE SCATTERING STRENGTH BY POLARIZATION:

Rough Surface Scattering	$ S_w > S_{HH} > S_{HV} $ or $ S_{VH} $
Double Bounce Scattering	$ S_{HH} > S_w > S_{HV} $ or $ S_{VH} $
Volume Scattering	Main source of $ S_{HV} $ and $ S_{VH} $

Table 2.2 Relative scattering strength by polarization

These general rules should help when comparing the RCS in different polarimetric channels. They can be applied to perform an automatic classification of scattering types if data with all relevant polarizations (i.e., quad-polarization data) are available. For more information on polarimetric SAR and polarimetric SAR data analysis, see Pottier & Lee 2009 and Van Zyl 2011.

An example of the information contained in quad-polarization SAR data is shown in Figure 2.10. There, the polarimetric scattering power of $|S_{HH}|$, $|S_{VV}|$, and $|S_{HV}|$ are presented in Figures 2.10(a), (b), and (c), respectively, for an ALOS PALSAR scene over Niamey, Niger. According to the rule above, strong scattering in $|S_{HH}|$ indicates a predominance of double-bounce scattering (e.g., stemmy vegetation, manmade structures), while strong $|S_{VV}|$ relates to rough surface scattering (e.g., bare ground, water), and spatial variations in $|S_{HV}|$ indicate the distribution of volume scatterers (e.g., vegetation and high-penetration soil types such as sand or other dry porous soils) across the scene. To enhance the visibility of differences between the channels, the HH, VV, and

HV information is often combined into a single RGB image, with $|S_{HH}|$ in red, $|S_{VV}|$ assigned to blue, and $|S_{HV}|$ in green. Such an RGB image composite for the scene over Niamey is shown in Figure 2.10(d). Extensive red areas can be seen in some urban districts (buildings) and some agricultural zones (stemmy vegetation). A patch of green can be seen to the south of Niamey, presumably relating to higher penetration sandy soils and the volumetric scattering on inclusion within the sand body. Most other areas have a tinge of blue, indicating bare soils.

2.3 Historic, Current, and Future SAR Sensors

Amazingly, spaceborne SAR sensors have been around for more than 40 years. The first SAR was

launched on June 28, 1978, on board NASA's Seasat satellite, a spaceborne platform aimed at monitoring oceanographic phenomena. As part of its sensor suite, Seasat carried an HH-polarized L-band SAR that was mounted at a fixed angle to observe global surface wave fields and polar sea ice conditions. Even though Seasat's SAR operated for only 106 days (a short circuit in the satellite's electrical system occurred on October 10, 1979), the mission was deemed an extensive success, demonstrating a SAR capability both ocean and land surface observation (Fu & Holt 1982).

Since the days of Seasat, SAR remote sensing has come a long way. Starting with ERS-1 in 1991, several SAR sensors with ever-improving imaging characteristics have been launched by an international community of satellite providers, collectively ensuring continuous coverage of the Earth with SAR data. Unfortunately, this international constellation of SAR systems comes with a downside. The SAR satellites launched by the various agencies vary widely in their sensor configurations such that data from different sensors are not always directly comparable (see Sec. 2.2). Section 2.3.1 outlines the main differences between different sensors in order to assist new users in choosing the correct SAR data for an intended application.

2.3.1 SAR SENSOR WAVELENGTHS

SAR sensors transmit energy in one of the micro-

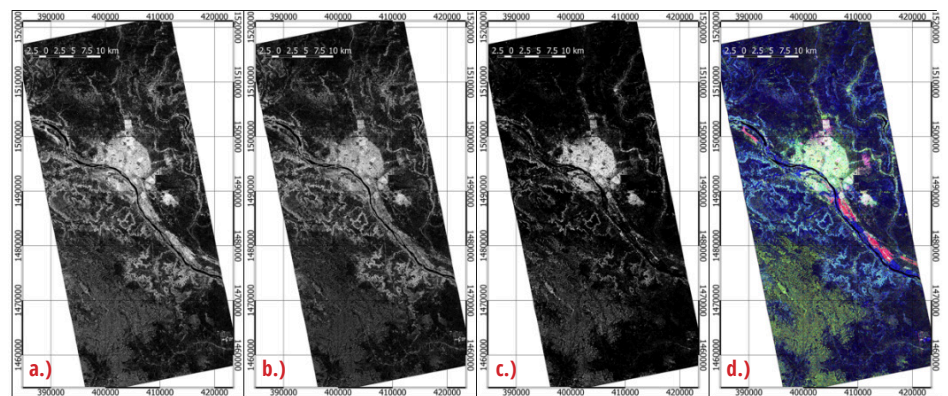


Figure 2.10 Fully-polarimetric L-band SAR scenes from the ALOS PALSAR sensor over Niamey, Niger: (a) $|S_{HH}|$, (b) $|S_{VV}|$, and (c) $|S_{HV}|$ scattering powers. An RGB color combination of these channels is shown in (d).

wave frequency bands shown in **Table 2.3**. Roughly speaking, radar systems use frequencies from 1 to 90 GHz, a spectral range that is subdivided into the frequency bands shown in the first column of **Table 2.3**. These bands were initially defined according to the different equipment needed to generate and detect signals at these particular wavelengths, but now, they can be understood as the equivalent of colors in the visual range. As microwave remote sensing was developed largely during World War II, a rather cryptic naming convention was used to disguise the meaning of microwave bands from the enemy. Unfortunately, this letter-based naming scheme (Ka-band to P-band) was never modified and may lead to confusion among new users of SAR.

Not all of the microwave bands shown in **Table 2.3** are used for SAR remote sensing. While some experimental airborne Ka- and Ku-band SAR systems exist, civilian spaceborne sensors have been exclusively using the lower frequency bands ranging from X- to P-band (blue shaded region in **Table 2.3**).

As explained in **Section 2.2**, the wavelength of a SAR sensor is intrinsically linked to the penetration

capabilities of the transmitted microwave signal, such that longer wavelength signals (e.g., signals at L- and P-band) penetrate deeper into vegetation canopies and soils. Hence, the applications supported by a SAR sensor depend on the SAR frequency band used.

Table 2.3 summarizes typical applications of SAR as a function of frequency band. It shows that sensors at X-band are predominantly used for urban and infrastructure monitoring. Due to the higher resolution capabilities of X-band radars, sensors at this frequency find broad application in surveillance and tracking and are also often used in the monitoring of industry installations. Due to the limited penetration into vegetation covers, X-band is rarely used for characterizing forest canopies for monitoring activity underneath vegetation.

With the predominate number of legacy systems operating at this frequency range, C-band sensors have been the workhorse of SAR monitoring over the last 30 years. With moderate- to high-resolution capabilities and increased vegetation penetration, C-band data can be seen as a good compromise between X-band and the longer wavelength L-band sensor classes. Compared to X-band SARs, C-band sensors typically allow

for wider swath imaging, lending themselves to regional- and global-scale applications. While C-band has improved canopy penetration capabilities, its signals will typically not penetrate all the way through a vegetation layer. Especially in regions with denser vegetation, C-band is of limited use for analyzing activity underneath canopy layers.

While S-band SAR sensors were rarely used in Earth observations in the past, this frequency will have increased usage in the near future. NovaSAR-S, an S-band SAR sensor, was launched in September 2018, and while access to NovaSAR-S data may be limited, it will provide some medium-resolution SAR data to explore the performance of S-band data for applications such as hazard monitoring, crop monitoring, forest monitoring (temperate and rainforests), as well as land-use mapping. More interesting to most users will be the upcoming NASA ISRO SAR satellite, NISAR. In addition to an L-band radar, NISAR will carry a fully polarimetric S-band SAR. While NISAR's S-band coverage will likely not be global, all data will be freely and openly available to the SAR science and applications community.

While most of the historic SAR systems operated

BAND	FREQUENCY		WAVELENGTH		TYPICAL APPLICATION
Ka	27 – 40	GHz	1.1 – 0.8	cm	Rarely used for SAR (airport surveillance)
K	18 – 27	GHz	1.7 – 1.1	cm	Rarely used (H ₂ O absorption)
Ku	12 – 18	GHz	2.4 – 1.7	cm	Rarely used for SAR (satellite altimetry)
X	8 – 12	GHz	3.8 – 2.4	cm	High-resolution SAR (urban monitoring; ice and snow, little penetration into vegetation cover; fast coherence decay in vegetated areas)
C	4 – 8	GHz	7.5 – 3.8	cm	SAR workhorse (global mapping; change detection; monitoring of areas with low to moderate vegetation; improved penetration; higher coherence); ice, ocean, maritime navigation
S	2 – 4	GHz	15 – 7.5	cm	Little but increasing use for SAR-based Earth observation; agriculture monitoring (NISAR will carry an S-band channel; expands C-band applications to higher vegetation density)
L	1 – 2	GHz	30 – 15	cm	Medium resolution SAR (Geophysical monitoring; biomass and vegetation mapping; high penetration; InSAR)
P	0.3 – 1	GHz	100 – 30	cm	Biomass. First P-band spaceborne SAR will be launched ~2020; vegetation mapping and assessment. Experimental SAR.

Table 2.3 Designation of microwave bands. Spaceborne SARs typically operate in the frequency bands shaded in green. Note: This table uses standard terminology common to the radar community. This nomenclature is not identical to ones used by other disciplines. For instance, P-band is often referred to as UHF band. Also note that the actual frequencies allocated for radar use by the International Telecommunications Union are narrower bands within these broad classifications.

in C-band, the family of future SAR sensors is largely focused on the L-band frequency range. While L-band SARs do not provide the high-resolution capabilities of shorter wavelength SARs, their ability to penetrate vegetation holds a number of advantages for Earth observation. With a higher likelihood of seeing the ground, L-band SARs are useful for mapping activity underneath canopies such as flooding. Due to the high penetration into vegetation covers, L-band SAR also lends itself well to characterizing canopy structure, especially in denser forests. Finally, the higher canopy penetration is also advantageous for users of Interferometric SAR (InSAR), achieving higher interferometric coherence (see [Sec. 2.6.2.](#)) and better deformation tracking capabilities.

P-band SAR sensors are currently under development. Spaceborne applications at this frequency are hampered by ionospheric distortions, and only recent developments in ionospheric correction (Belcher 2008, Belcher and Rogers 2009, Gomba et al. 2016, Jehle et al. 2010, Jehle et al. 2009, Kim et al. 2011, Meyer et al. 2006, Meyer & Nicoll 2008a, Meyer 2011, Meyer et al. 2016, Meyer & Nicoll 2008b, Pi et al. 2012) have allowed spaceborne P-band SAR missions to go forward. The first spaceborne P-band SAR—ESA’s Biomass mission—is planned to launch in 2021 and will focus on mapping the status and the dynamics of Earth’s forests, as represented by the distribution of forest biomass and its changes.

2.3.2 A SUMMARY OF RELEVANT SAR PLATFORMS WITH THEIR PROPERTIES

A list of the most relevant past, current, and future SAR platforms is provided in [Table 2.4](#). The sensors are sorted by their period of performance. For each instrument, the sensor wavelength, supported polarization modes, resolution and size of image products, repeat cycle, and means of data access are listed. This quick guide may be useful in selecting appropriate sensors for a specific application.

2.4 SAR Data Types and Their Applications

[Table 2.4](#) showcases the diversity of SAR sensors that have been launched since the beginning of the

spaceborne SAR era in 1979. While the deep, multitemporal archive provided by these sensors is of tremendous value for users interested in long-term Earth observation, SAR data products from these various platforms are, unfortunately, plagued by inconsistent naming conventions and come in a range of data types and formats, which can cause confusion even for more senior users of SAR. The following sections attempt to summarize and categorize the various data types and nomenclatures used by different data providers to provide guidance to users new to this tremendously useful Earth observation asset. For every data type, typical naming conventions are listed and appropriate open source software tools are introduced. Also summarized are the main applications associated with a specific data type. A concise summary of all information provided can also be found in [Table 2.5](#).

The variety of data types provided by a SAR system are related to the diverse flavors of information that are captured in every SAR acquisition. In every pixel, a SAR provides measurements of signal amplitude, phase, and polarization, all of which are related to different physical quantities of the observed ground. As extracting and utilizing these different information layers is often not straightforward—and as amplitude, phase, and polarization information is often relevant to different user communities—SAR data providers have decided to offer their imagery up in a range of different processing levels, each progressively simplified and tailored to emphasize different components of the SAR information space.

2.4.1 SAR RAW DATA

General Description: As the purest of all SAR processing levels, RAW data corresponds to the decoded but otherwise unfocused (i.e., Wiley’s aperture synthesis processing has not yet been applied; [Sec. 2.1.3](#)) raw observables made by a SAR sensor. Unlike optical sensors, visualizing raw SAR data does not provide much useful information about the scene. Only after aperture synthesis processing is the RAW data transformed into an interpretable image.

Applications: RAW data products are the basis for all higher level SAR processing levels, and as such, RAW is an essential data type in every SAR data

archive. Outside of the user community interested in SAR data processing, however, RAW products find very little use. Interestingly, while RAW data are an essential product for every SAR sensor, not every satellite operator has decided to make his RAW data products available to the community. For some sensors, satellite data security laws prohibit the publication of RAW data products. Mostly, however, sensor providers elect to hide RAW data to retain proprietary information about their SAR processing routines.

Naming Convention: RAW products are categorized as processing Level 0 data, a processing level typically abbreviated as L0. An exception to this abbreviation exists for data from the ALOS PALSAR sensor, which uses L1.0 when referring to their RAW data products.

Open Source Software Tools: There are a number of open source software tools that can be used to read and manipulate (focus) RAW SAR data products. These include the following:

- **InSAR Scientific Computing Environment (ISCE)**—Developed by Jet Propulsion Laboratory (JPL)/Stanford/Caltech. More information and download: <https://winsar.unavco.org/isce.html>.
- **GMTSAR**—Developed by Scripps Institution of Oceanography. More information and download: <http://topex.ucsd.edu/gmtsar/>.
- **Repeat Orbit Interferometry PACKage (ROI_PAC)**—Developed by JPL/Caltech. More information and download: https://winsar.unavco.org/portal/wiki/ROI_PAC/.
- **Delft Object-oriented Radar Interferometric Software (DORIS)**—Developed by Delft University of Technology. More information and download: <http://doris.tudelft.nl/>.

Note that most of these tools are focused on the SAR expert community and therefore require a considerable amount of expertise to use correctly. Furthermore, these tools predominantly reside on Linux or UNIX operating systems and use command-line methods as the means of user interaction.

2.4.2 SINGLE LOOK COMPLEX IMAGE

General Description: Single Look Complex (SLC) images are fully focused SAR data that are

SENSOR	LIFETIME	WAVELENGTH/ FREQUENCY	POLARIZATION	RESOLUTION	FRAME SIZE	REPEAT CYCLE	ACCESS
Seasat	1978	L-band $\lambda = 24.6\text{cm}$	HH	Az: 25m Rg: 25m	100km	-	Free & open
ERS-1	1991-2001	C-band $\lambda = 05.6\text{cm}$	W	Az: 6-30m Rg: 26m	100km	35 days	Restrained
JERS-1	1995-1998	L-band $\lambda = 24.6\text{cm}$	HH	Az: 18m Rg: 18m	75km	44 days	Restrained
ERS-2	1995-2011	C-band $\lambda = 05.6\text{cm}$	W	Az: 6-30m Rg: 26m	100km	35 days	Restrained
ENVISAT	2002-2012	C-band $\lambda = 05.6\text{cm}$	HH, W, W/HH, HH/HV, W/VH	Az: 28m Rg: 28m	100km	35 days	Restrained
ALOS-1	2006-2011	L-band $\lambda = 24.6\text{cm}$	FBS: HH, W FBD: HH/HV, HH/VH PLR: HH/HV /VH /W ScanSAR: HH, W	FBS: 10x10m FBD: 20x10m PLR: 30x10m ScanSAR: 100m	FBS: 70km FBD: 70km PLR: 30km ScanSAR: 250-350km	46 days	Free & open
Radarsat-1	1995-2013	C-band $\lambda = 05.6\text{cm}$	HH	Standard: 25x28m Fine: 9x9m Wide1: 35x28m Wide2: 35x28m ScanSAR: 50x50-100x100m	Standard: 100km Fine: 45km Wide1: 165km Wide2: 150km ScanSAR: 305-510km	24 days	1995-2008: Restrained 2008-2013: Commercial
TerraSAR-X TanDEM-X	2007- 2010-	X-band $\lambda = 03.5\text{cm}$	Single: HH, W Dual: HH/W, HH/HV, W/VH Twin: HH/W, HH/VH, W/VH	Spotlight: 0.2x1.0-1.7x3.5m Stripmap: 3x3m ScanSAR: 18-40m	Spotlight: 3-10km Stripmap: 50x30km ScanSAR: 150x100-200x200km	11 days	Application-dependent; restrained scientific, commercial
Radarsat-2	2007-	C-band $\lambda = 05.6\text{cm}$	Single: HH, W, HV, VH Dual: HH/HV, W/VH Quad: HH/HV/VH/W	Spotlight: ~1.5m Stripmap: ~3x3-25x25m ScanSAR: 35x35-100x100m	Spotlight: 18x8km Stripmap: 20-170m ScanSAR: 300x300- 500x500km	24 days	Commercial
COSMO -SkyMed	2007-	X-band $\lambda = 03.5\text{cm}$	Single: HH, W, HV, VH Dual: HH/HV, HH/W, W/VH	Spotlight: $\leq 1\text{m}$ Stripmap: 3-15m ScanSAR: 30-100m	Spotlight: 10x10km Stripmap: 40x40km ScanSAR: 100x100 - 200x200km	Satellite: 16 days Constellation: ~hrs	Commercial; limited proposal- based scientific
ALOS-2 PALSAR-2	2014-	L-band $\lambda = 24.6\text{cm}$	Single: HH, W, HV, VH Dual: HH/HV, W/VH Quad: HH/HV/VH/W	Spotlight: 1x3m Stripmap: 3-10m ScanSAR: 25-100m	Spotlight: 25x25km Stripmap: 55x70-70x70km ScanSAR: 355x355km	14 days	Commercial; limited proposal- based scientific
Sentinel-1	2014-	C-band $\lambda = 05.6\text{cm}$	Single: HH, W Dual: HH/HV, W/VH	Stripmap: 5x5m Interferometric Wide Swath (IW): 5x20m Extra Wide Swath (EW): 20-40m	Stripmap: 375km IW: 250km EW: 400km	Satellite: 12 days Constellation: 6 days	Free & open
SAOCOM	2018-	L-band $\lambda = 24.6\text{cm}$	Single: HH, W Dual: HH/HV, W/VH Quad: HH/HV/VH/W	Stripmap: 10x10m TopSAR: 100x100m	Stripmap: >65km TopSAR: 320km	Satellite: 16 days Constellation: 8 days	TBD
PAZ SAR	2018-	X-band $\lambda = 03.5\text{cm}$	*See TerraSAR/TanDEM-x	*See TerraSAR/TanDEM-x	*See TerraSAR/TanDEM-x	11 days	Commercial
RCM	2019	C-band $\lambda = 05.6\text{cm}$	Single: HH, W, VH, HV Dual: HH/HV, W/VH, HH/W Compact Quad	Very high, high, medium, and low-res modes (3-100m)	20x20-500x500km	Satellite: 12 days Constellation: ~hrs	TBD
NISAR	2021	L-band $\lambda = 24.6\text{cm}$	Single: HH, W, VH, HV Dual: HH/HV, W/VH, HH/W Quad	3-20m (mode dependent)	250km	12 days	Free & open
BIOMASS	2021	P-band $\lambda = 70.0\text{cm}$	Quad	$\leq 60 \times 50\text{m}$	160km	17 days	Free & open
TanDEM-L	2023	L-band $\lambda = 24.6\text{cm}$	Single, dual, quad modes	12x12m	350km	Satellite: 16 days Constellation: 8 days	Free & open

Table 2.4 List of past, current and upcoming spaceborne SAR sensors with their properties.

SENSOR	FORMAT	PRODUCT NAME	PRODUCT FILES	PROCESSING LEVEL	OPEN SOURCE TOOLS	APPLICATIONS
CURRENT SPACEBORNE SENSORS						
Seasat	HDF5	L1 HDF5 Image	h5, xml, kml, jpg, qc_report	Amplitude	ASF MapReady, QGIS	Visualization; GIS-compatible
	GeoTIFF	L1 GeoTIFF	tif, xml, kml, jpg, qc_report	Geocoded amplitude	QGIS; graphics software	Visualization; GIS-compatible
ERS-1&2 Envisat Radarsat-1 JERS-1	EOS	L0	D,L,P, kml, jpg	Raw	N/A	Production of higher-level products
		L1 Image		Amplitude	ASF MapReady; S1TBX	Visualization, mapping, change detection
ALOS-1	CEOS	L1.0	LED, IMG, VOL, TRL	Raw	N/A	Production of higher-level products
		L1.1 Complex		SLC	SNAP; ROI_PAC; DORIS; PolSARpro; GMTSAR	Interferometry
		L1.5		Amplitude	ASF MapReady; S1TBX; PolSARpro	Visualization, mapping, change detection
TerraSAR-X TanDEM-X	COSAR format	L1 SSC (Single Look Slant Range Complex)		SLC	SNAP; ROI_PAC; DORIS; PolSARpro; GMTSAR	Interferometry
	GeoTIFF	L1 MGD (Multi Look Ground Range Detected)		Amplitude	ASF MapReady; SNAP; PolSARpro	Visualization, mapping, change detection
	GeoTIFF	L1 GEC (Geocoded Ellipsoid Corrected)		Amplitude	ASF MapReady; SNAP; PolSARpro	Visualization, mapping, change detection
	GeoTIFF	L1 EEC (Enhanced ellipsoid corrected)		Amplitude	ASF MapReady; SNAP; PolSARpro	Visualization, mapping, change detection
Radarsat-2	GeoTIFF or NITF 2.1 with XML	L1 SLC		SLC	SNAP; ROI_PAC; DORIS; PolSARpro; GMTSAR	Interferometry
		L1 Ground Range (SGX; SGF; SCN; SCW; SCF; SCS)		Amplitude	SNAP; PolSARpro	Visualization, mapping, change detection
		L1 Geocorrected (SSG; SPG)		Amplitude	SNAP; PolSARpro	Visualization, mapping, change detection
COSMO-SkyMed	HDF5	L0 RAW		Raw		Production of higher-level products
		L1A		SLC	SNAP; ROI_PAC; DORIS; PolSARpro; GMTSAR	Interferometry
		L1B MDG (Multi-look Detected Ground Range)		Amplitude	SNAP; PolSARpro	Visualization, mapping, change detection
		L1C GEC		Amplitude	SNAP; PolSARpro	Visualization, mapping, change detection
		L1D GTC (Geocoded Terrain Corrected)		Amplitude	SNAP; PolSARpro	Visualization, mapping, change detection
		Various higher-level products				
ALOS-2 PALSAR-2		L1.1 SLC		SLC	SNAP; ROI_PAC; DORIS; Pol-SARpro; GMTSAR	Interferometry
		L1.5 (slant-range detected)		Amplitude	SNAP; PolSARpro	Visualization, mapping, change detection
		L2.1 GTC		Geocoded amplitude	SNAP; PolSARpro	Visualization, mapping, change detection
		L3.1 (Quality corrected L1.5)		Enhanced amplitude	SNAP; PolSARpro	Visualization, mapping, change detection
Sentinel-1	SAFE	L0 raw data	tiff, xml, xsd, kml, html, png, pdf, safe	Raw	N/A	Production of higher-level products
	GeoTIFF	L1 SLC		SLC	S1TBX; ROI_PAC; DORIS; PolSARpro	Interferometry
	GeoTIFF	L1 Detected High-Res Single- & Dual-Pol		Georeferenced Amplitude	ASF MapReady; Google Earth Engine; S1TBX; PolSARpro	Visualization, mapping, change detection
	GeoTIFF	L1 Detected Single- & Dual-Pol		Georeferenced Amplitude	ASF MapReady; Google Earth Engine; S1TBX; PolSARpro	Visualization, mapping, change detection

Table 2.5 Current and upcoming spaceborne SAR sensors with their properties.

SENSOR	FORMAT	PRODUCT NAME	PRODUCT FILES	PROCESSING LEVEL	OPEN SOURCE TOOLS	APPLICATIONS
RECENT AND FUTURE SPACEBORNE SENSORS						
SAOCOM PAZ SAR RCM NISAR BIOMASS TanDEM-L					Formats and data types yet to be determined	
AIRBORNE SENSORS						
UAVSAR PolSAR	UAVSAR	Ground Projected Complex [full-res; 3x3; 5x5]	grd, ann	Georeferenced Amplitude	ASF MapReady; PolSARpro	Visualization
		Multi-Look Complex	mic, ann	MLC	ASF MapReady; PolSARpro	Polarimetry
		Compressed Stokes Matrix	dat, ann	AIRSAR compressed stokes matrix	ASF MapReady; PolSARpro	Polarimetry
	GeoTIFF	Pauli Decomposition	tif	MLC pol. decomposition	QGIS; graphics software	Visualization, GIS compatible
	KMZ	Google Earth KMZ	kmz	KML compressed	Google Earth	Visualization
UAVSAR InSAR	UAVSAR	Amplitude	amp1, amp2, ann	Amplitude	ASF MapReady; PolSARpro	Visualization
		Ground Projected Amplitude	amp1.grd, amp2.grd, hgt.grd, ann	Georeferenced Amplitude	ASF MapReady; PolSARpro	Visualization
		Interferogram	int, unw, cor, ann	Interferogram	ASF MapReady; PolSARpro	
		Ground Projected Interferogram	cor.grd, hgt.grd, int.grd, unw.grd, ann	Interferogram	ASF MapReady; PolSARpro	
	KMZ	Google Earth KMZ	amp.kmz, cor.kmz, hgt.kmz, int.kmz, osr.kmz, unw.kmz		Google Earth	Visualization

Table 2.5, continued

provided at the full native resolution (single look) with both amplitude and phase information stored in each (complex) pixel. SLC products are typically provided in the original slant-range observation geometry (Fig. 2.1) and are therefore not geocoded or terrain-corrected. In contrast to most optical sensors, the native resolution of SAR sensors is often significantly different along the azimuth and range image directions. Hence, SLC images often look geometrically distorted when viewed in image processing software. While SLCs usually come with radiometric calibration factors already applied, speckle noise remains unmitigated in these full-resolution products. For polarimetric data, separate SLC products are provided for each polarimetric channel.

Applications: The phase information stored in SLC products is an essential prerequisite for InSAR processing (Sec. 2.6.2), which is used for mapping surface topography or surface deformation. In addition to its use in InSAR, SLCs are also the basis for

higher level image products such as amplitude images, polarimetric products, and geocoded images. See Table 2.5 for more information.

Naming Convention: In the SAR world, SLC products are categorized as processing Level 1 data, typically abbreviated as L1 or L1 SLC data. An exception to this abbreviation exists for data from the ALOS PALSAR sensor, which uses L1.1 when referring to its SLC products.

Open Source Software Tools: SLC data can be read and further processed by a series of open source software tools. These include (but are not limited to) the following:

- All previously named RAW data tools (ISCE, ROI_PAC, GMTSAR, DORIS)
- **MapReady:** Developed by the Alaska Satellite Facility. More information and download: <https://www.asf.alaska.edu/data-tools/mapready/>.
- **Sentinel Application Platform**

(SNAP): Developed by ESA. More information and download: <http://step.esa.int/main/download/>.

While all of these tools are capable of processing SLC products, not all tools work with all sensors. Users should refer to the links above to ensure that their data can be successfully processed with a particular tool choice.

2.4.3 DETECTED (AMPLITUDE) IMAGES

General Description: Amplitude products are fully focused SAR images that have been stripped of phase information and are typically multi-looked (spatially averaged) to reduce speckle noise and to create pixels of approximately square size. While useful for a range of mapping and monitoring applications, amplitude products unfortunately come in a variety of geocoding stages. Most legacy SAR systems (e.g., ERS-1/2, Envisat, Radarsat-1, JERS-1, and ALOS PALSAR) provide non-geocoded amplitude products

that are left in the original acquisition geometry, and it is upon the user to geocode these datasets manually. Other sensors (e.g., Sentinel-1) make georeferenced amplitude products available. While these products remain in their native acquisition geometry, information needed to link the image coordinate system to geographic coordinates is stored within the image file. Currently, only the recently reprocessed archive of Seasat (available at the Alaska Satellite Facility) provides data in full geocoded formats.

Note that amplitude products are typically georeferenced or geocoded to an ellipsoidal approximation of the Earth. This means that image distortions caused by surface topography (see [Fig. 2.4](#)) are not corrected in amplitude products.

Applications: In their original form, the main applications of amplitude images are limited to visualization and data inspection. Only after an end user applies geocoding and terrain correction steps do these products have relevance in mapping, change detection, hazard monitoring, and other Earth observation disciplines.

Naming Convention: Amplitude products belong to the L1 family of products. To distinguish them from SLCs, they are often referred to as L1.5 (ALOS PALSAR) or L1 Detected (Sentinel-1, ERS-1/2, Envisat, Radarsat-1, JERS-1). While data are provided in a range of custom formats, most modern sensors increasingly favor standard formatting such as GeoTIFF or HDF5. For more information, please refer to [Table 2.5](#).

Open Source Software Tools: Amplitude products can be read and further processed by all of the software tools mentioned in [Section 2.4.2](#) and [Table 2.5](#).

2.4.4 POLARIMETRIC PRODUCTS

General Description: Most SAR sensors provide the different channels (i.e., HH, HV, VH, and VV; see [Sec. 2.2.3](#)) of multi-polarization data as separate layers, processed to either an L0, L1 SLC, or L1 Detected product. There are, however, some exceptions to this general approach. The NASA JPL-run airborne remote sensing system UAVSAR offers two product types (the Compressed Stokes Matrix and Pauli Decomposition products) that are true po-

larimetric products. The Compressed Stokes Matrix captures information about the polarization state of the measured polarimetric signal, while the Pauli Decomposition provides information on the polarimetric scattering properties of an observed surface. Polarimetric products are also planned for upcoming SAR missions NISAR and TanDEM-L.

Applications: Polarimetric data are useful for studying the structure of the observed surface and performing unsupervised image classifications. Polarimetric products have been used extensively in agriculture monitoring (crop classification, soil moisture extraction, and crop assessment) (Alemohammad et al. 2016, Jagdhuber et al. 2013, Liu et al. 2013, Quegan et al. 2003, Xie et al. 2015), oceanography (surface currents and wind field retrieval) (Hooper et al. 2015, Latini et al. 2016, Migliaccio & Nunziata 2014), forestry (forest monitoring, classification, and tree height estimation) (Banqué et al. 2016, Mitchard et al. 2011, Shimada et al. 2016, Walker et al. 2010), disaster monitoring (oil spill detection and disaster assessment), and military applications (ship detection and target recognition/classification).

Naming Convention: Due to the recent development of standalone polarimetric products, no naming convention has been established thus far.

Open Source Software Tools: Polarimetric data can be processed with the following software packages (sorted in ascending order of sophistication of available polarimetric processing):

- **MapReady**—Developed by the Alaska Satellite Facility. More information and download: <https://www.asf.alaska.edu/data-tools/mapready/>.
- **SNAP (Sentinel Application Platform)**—Developed by ESA. More information and download: <http://step.esa.int/main/download/>.
- **PolSARpro**—Developed by ESA. More information and download: <https://earth.esa.int/web/polsarpro/home>.

2.4.5 LEVEL 2 AND HIGHER LEVEL PRODUCTS

General Description: For the sake of this handbook, Level 2 data are defined as all data products that are projected to the ground, gridded in regular grids, and transformed into physical variables such as

a calibrated radar cross section (e.g., the radiometric terrain-corrected data generated via the processing flow described in [Sec. 2.6.1](#)), line-of-sight deformation, or polarimetric decomposition variables.

While Level 2 products are offered by only a few missions at this point in time, an increasing number of future sensors will offer products at advanced processing levels. Currently, operationally produced Level 2 products are only provided for the Seasat and the UAVSAR archive and include geocoded amplitude images (both sensors) as well as polarimetric and interferometric products (UAVSAR; [Table 2.4](#)).

Several data formats have been used for Level 2 and higher products from SAR, as no common data format has been established yet for this still uncommon product type. Currently used formats include GeoTIFF, HDF5, and KMZ.

Applications: Level 2 SAR data products facilitate a wide range of applications. Calibrated amplitude images find use in a range of fields such as general mapping, land-use classification, change detection, and hazard analysis. Interferometric data may be used in damage mapping, geophysical analyses of surface deformation, and more.

Naming Convention: Various.

Open Source Software Tools: The geocoded products can be used in most Geographic Information System (GIS) tools. While GeoTIFF products are natively compatible with GIS tools, readers may have to import HDF5 formats with their respective meta-data information.

2.5 Accessing SAR Data

While an increasing number of satellite systems are operating under a free and open data policy, many legacy sensors and some currently operating higher resolution sensors are still providing data under a restricted or commercial paradigm. The following sections provide information on how, where, and under which conditions data from these different types of sensors can be accessed.

2.5.1 FREE AND OPEN DATA POLICY MISSIONS

Past and current SAR missions that have (at the writing of this chapter) adopted a free and open data

policy include the spaceborne sensors Seasat, ERS-1/2, ALOS-1, and Sentinel-1, as well as the NASA-operated airborne SARs AirSAR, UAVSAR, and AIRMOSS. Upcoming missions also expected to provide data in a free and open manner include the Canadian Radarsat Constellation Mission (RCM), NASA's NISAR, DLR's TanDEM-L, and ESA's Biomass mission. Means of data access for these sensors is briefly described in the following sections. A summary of data access to free and open SAR sensors is provided in **Table 2.6**.

2.5.1.1 Accessing Data from the ERS-1/2 and Envisat Missions

With a combined lifetime from 1991 until 2011, the ERS system (composed of ERS-1 and ERS-2) provides unique insights into 20 years of changes on the Earth's surface. Therefore, it remains a relevant data source for those interested in climate change, hazard monitoring, and environmental analysis.

Two means of accessing data from this long-lived legacy SAR system are:

- **ESA Simple Online Catalogue**—The global archive of the ERS and Envisat systems can be searched and ordered via the ESA-maintained [Simple Online Catalogue](#). ESA SOC replaced the EOLI-SA (Earth Observation Link – Stand Alone) browser in early 2019. Once relevant data are identified, images can be downloaded by the user free of charge once reproduction is completed, with the possibility of additional data downloads depending on overall system availability.
- **ASF Vertex**—Alternately, a subset of the available ERS SAR data is available through the services of the NASA Alaska Satellite Facility (ASF) Distributed Active Archive Center (DAAC). Level 0 and L1.5 data over North America ([ASF station mask](#)) are freely and openly available through [ASF's Vertex](#) client for immediate download. See **Figure 2.11** for a view of the ASF Vertex interface. Note that the ASF archive does not include data from the Envisat mission.

2.5.1.2 ALOS-1 PALSAR

Data from JAXA's ALOS-1 PALSAR sensor are available through a distributed set of data nodes that

MISSION(S)	REGION	DATA ACCESS	REQUIREMENTS
Seasat	Global	ASF Vertex	One-time registration
ERS-1&2, ENVISAT	Global	ESA Simple Online Catalogue	PI proposal
	ASF Station Mask (ERS only)	ASF Vertex	One-time registration
ALOS-1 PALSAR	Americas/Antarctica	ASF Vertex	One-time registration
	Europe/Africa/Greenland	ALOS PALSAR On-The-Fly	PI proposal
	Asia	AUIG2	PI proposal
	Australia/Oceania	Unknown	Unknown
Sentinel-1	Global	ASF Vertex ESA's Copernicus Open Access Hub	One-time registration
AIRSAR, UAVSAR	Limited extent	ASF Vertex	One-time registration
AirMOSS	Limited extent	ORNL DAAC	One-time registration

Table 2.6 List of free and open SAR sensors with modes of data access.

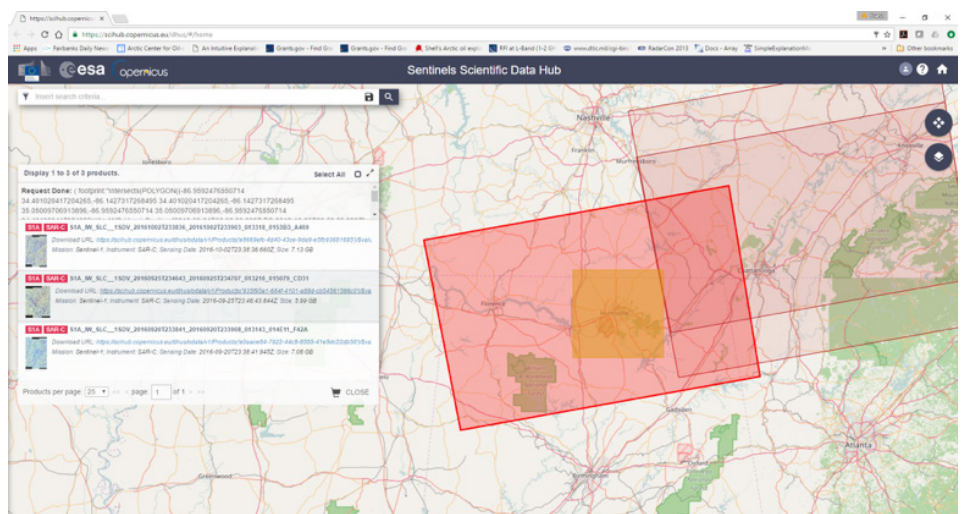
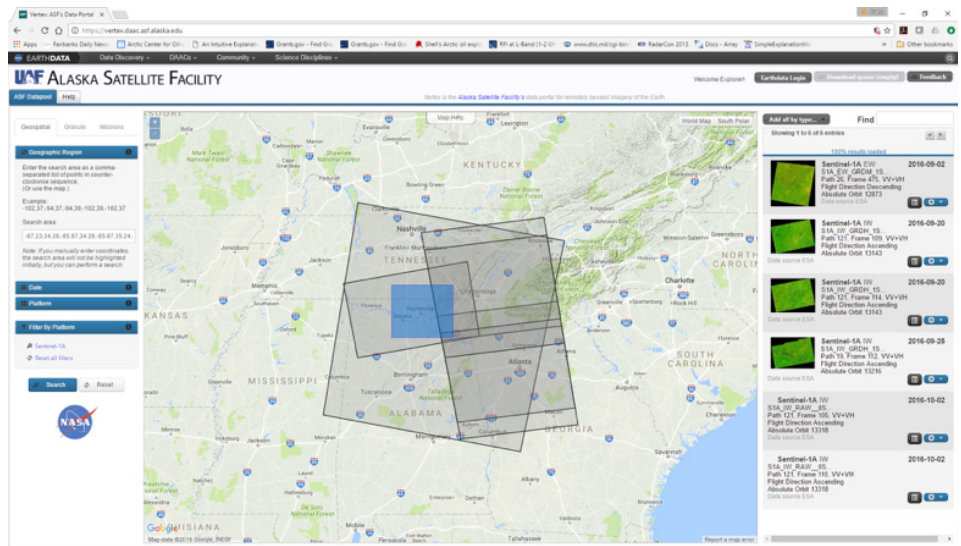


Figure 2.11. A look at the interfaces of two major SAR data search clients: (a) ASF Vertex client and (b) ESA Copernicus Open Access Hub. Both clients allow for convenient data search via a map interface.

were originally established to make access to ALOS data more effective for end users. Separate data centers are available for the Americas (data located at ASF; free and open access via [ASF Vertex](#)), Europe and Africa (ESA; Principal Investigator (PI) proposal needed; access via [ALOS PALSAR On-The-Fly web interface](#)), Asia (JAXA; PI proposal needed; access via ALOS User Interface Gateway ([AUIG2](#))), and Australia/Oceania (Geoscience Australia; data access via JAXA's [AUIG2](#)).

In 2015, data from the ALOS-1 PALSAR sensor became [unrestricted](#), enabling all ALOS data nodes to provide data freely and openly to its users. While ASF has fully implemented this data policy—ALOS PALSAR data over the Americas are now freely and openly available through ASF's Vertex client—other data nodes are still working on implementing this unrestricted data policy.

2.5.1.3 Sentinel-1

The Sentinel-1 mission is the first of the six Sentinel-dedicated missions operated by the European Copernicus programme. Sentinel-1 is based on a constellation of two SAR satellites to ensure continuity of C-band SAR observations across the globe. Sentinel-1A was launched on April 3, 2014, and the second Sentinel-1 satellite, Sentinel-1B, was launched on April 25, 2016.

The operational nature of Sentinel-1 is a game changer in a number of application domains thanks to the large-scale mapping capability and revisiting frequency of the two identical satellites, together with a high-capacity ground segment that systematically processes, archives, and makes available all the generated data products to users online in a routine operational way (Potin et al. 2016).

The growing global archive of Sentinel-1 is accessible through two freely available search clients:

- **ESA's Copernicus Open Access Hub:** The global archive of the Sentinel-1 SAR constellation can be accessed via [ESA's Copernicus Open Access Hub](#). Requiring only a simple, one-time registration, this hub allows for quick and easy data download via an interactive map interface. In addition to Sentinel-1, the Copernicus Open Access Hub also provides access

MISSION(S)	REGION	DATA ACCESS	REQUIREMENTS
ALOS-2 PALSAR-2	Global	Commercial: PASCO	Price list
		Science: AUIG2	Proposal to JAXA
Radarsat-1&2	Global	Commercial: MDA	MDA price list
	North America	Science: ASF Vertex	Proposal to NASA
COSMO-SkyMed	Global	Commercial: e-goes	e-goes price list
		Science: ASI	Proposal to ASI
TerraSAR-X, TanDEM-X	Global	Commercial: Airbus	Airbus price list
		Science (reduced cost): TSX / IDX	Proposal to DLR (TSX / IDX)
		Archived data (free): TSX	Proposal to DLR

Table 2.7 List of restricted/commercial SAR sensors with modes of data access.

to all other Sentinel missions (at the time of writing, access to Sentinel-1 to Sentinel-3 is possible), making it a convenient one-stop-shop for users interested in multi-sensor Earth observation data. A screenshot of the Copernicus Open Access Hub interface is shown in [Figure 2.11](#).

- **ASF Vertex:** The global Sentinel-1 archive is also available through the previously mentioned [ASF Vertex](#) client ([Fig. 2.11](#)). Similar to the Copernicus Open Access Hub, data can be searched via a convenient map interface. In addition to Sentinel-1, ASF Vertex provides free and open access to other SAR data such as those from the ERS, UAVSAR, AirSAR, and Seasat missions.
- **Google Earth Engine:** In addition to the previous options, geocoded Sentinel-1 Detected (Amplitude) products are now available through [Google Earth Engine](#) (GEE). While GEE does not allow downloading of Sentinel-1 image products, it provides a convenient cloud-based analysis platform within which Sentinel-1 data can be analyzed together with data from optical sensors. Hence, GEE may allow new users of SAR to gain experience with this dataset without requiring local software installs and without having to download large volumes of SAR data.

2.5.1.4 NASA's Open Access Airborne SAR Sensors

Data from the NASA airborne SAR sensors AIR-

SAR (C-, L-, and P-bands; 1990–2004) and UAVSAR (L-band; 2008–present) are accessible through the ASF Vertex client ([Fig. 2.11](#)). While covering only limited areas, the versatility and high resolution of these sensors make them interesting for a range of Earth observation disciplines. UAVSAR data are also available at JPL, which is also operating the mission. To download data directly from JPL, please visit <https://uavsar.jpl.nasa.gov/>.

Currently, AirMOSS data (P-band; 2012–present) are being offered through the NASA Oak Ridge National Laboratory (ORNL) DAAC. To access AirMOSS data from ORNL, please visit https://daac.ornl.gov/cgi-bin/dataset_lister.pl?p=36.

2.5.2 RESTRICTED-ACCESS AND COMMERCIAL SAR MISSIONS

Despite their largely commercial nature, there are means to access certain data from the Radarsat-1 and -2, TerraSAR-X, TanDEM-X, COSMO-SkyMed, and ALOS-2 PALSAR-2 missions at low cost. Detailed information on these individual sensors is provided in [Table 2.7](#) and the following paragraphs.

2.5.2.1 Radarsat-1 and -2

Radarsat-1 and -2 are Canada's staple SAR sensors which have been continuously providing C-band medium- to high-resolution SAR data since 1995. Since the launch of Radarsat-2 in 2007, most of the combined Radarsat archive has migrated to a commercial data policy with data access fees above \$1,000 CAD per image frame. Information on the data costs for Radarsat-1 and -2 datasets can be found from the com-

mercial distributor [MDA](#). On occasion, low-cost data access is granted to Canadian and European PIs under the [Science and Operational Applications Research for Radarsat-2 \(SOAR\)](#) program after a competitive PI proposal is approved.

Outside of this general agreement, some limited Radarsat-1 data (from the period of 1995–2009) are also available through the NASA ASF DAAC under a restricted data access agreement and can be discovered through its ASF Vertex search client. To access ASF-held Radarsat-1 data, a proposal to NASA is necessary. Once approved, data can be accessed free of charge. More on ASF's Radarsat-1 restricted data use agreement [here](#) at this link.

2.5.2.2 ALOS-2 PALSAR-2

While ALOS-2 PALSAR-2 data are distributed commercially by the PASCO Corporation, a limited amount of data is provided for free to the science community. To apply for limited free data access (50 scenes per year), look for regularly released [ALOS Research Announcements](#). A proposal describing the research effort is needed and is reviewed for validity. If approved, free data access to up to 50 scenes per year is granted via the [AUIG2](#) interface. Information about the data costs for commercial ALOS-2 PALSAR-2 data can be found [here](#).

2.5.2.3 High-Resolution X-band SAR Data from TerraSAR-X, TanDEM-X, and COSMO-SkyMed

While the high-resolution X-band SAR sensors TerraSAR-X, TanDEM-X, and COSMO-SkyMed provide most of their data under a commercial license, similar to ALOS-2 PALSAR-2, some limited data can be accessed at a low cost (or for free) once a PI proposal is reviewed and approved.

Information on how to access commercial data from the TerraSAR-X and TanDEM-X missions (including pricing information) is available from the [Airbus Defense and Space Company](#) website. For information on how to apply for access to low-cost science use data, see the [TerraSAR-X Science Server](#) or, accordingly, the [TanDEM-X Science Server](#). While proposals to access archived TerraSAR-X data can always be submitted, look for special announcements of opportunities to

apply for access to newly acquired or special mission phase data. Through the TanDEM-X Science Server, users can also apply for segments of the TanDEM-X Digital Elevation Model (DEM) in addition to the SAR images themselves.

Information on commercial access to COSMO-SkyMed data can be retrieved from their commercial vendor, [e-geos](#). Reduced-rate science data access is available regularly through COSMO SkyMed Constellation Data Utilization announcement of opportunities. Please check for upcoming opportunities on the [Italian Space Agency \(ASI\)](#) webpage.

2.6 SAR Image Processing Routines – Theory

2.6.1 GEOCODING AND RADIOMETRIC TERRAIN CORRECTION

2.6.1.1 Theoretical Background

Due to the side-looking observation geometry, SAR images are subject to geometric and radiometric distortions ([Sec. 2.1.4](#)). In addition to the geometric mislocation of pixels in topographically inclined areas, the oblique angle of the illuminating radar energy adds topographic shading to the true surface RCS, giving the sensor-facing side of hill slopes a radiometrically “overexposed” appearance (see [Figure 2.12\(a\)](#)). Both of these effects hamper the use of SAR for many applications. The radiometric modulations often disguise the true radar reflectance of the observed scene, reducing the applicability of SAR for studying the properties of the surface. Furthermore, geometric and radiometric distortions make the application of SAR for change detection more difficult, as these highly incidence angle-dependent artifacts lead to classification errors if images with different observation geometries are combined. Hence, correction of geometric and radiometric distortions is advisable if SAR data are to be analyzed together with other image data or across datasets with varying incidence angles.

The RCS of a pixel in a calibrated SAR image is composed of:

$$\sigma = \sigma^0(\theta_i) \cdot A_\sigma(\theta_i), \quad (2.9)$$

where σ^0 is the (incidence angle-dependent) normal-

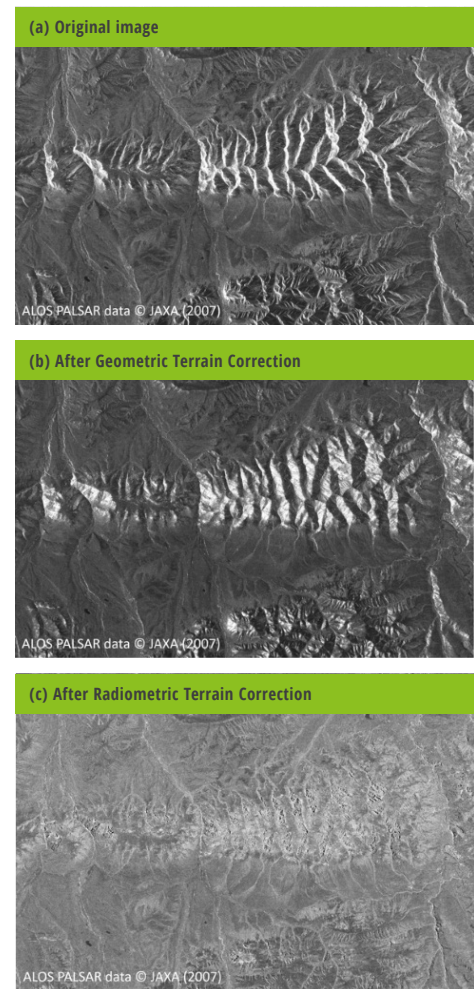


Figure 2.12 Example of geometric (b) and radiometric (c) normalization applied to an ALOS PALSAR image over Alaska (a). The applied corrections enable the use of SAR data in GIS environments (geometric correction step), provide physically correct RCS values for every pixel, and enable unbiased change detection from multiple observation geometries.

ized RCS, θ_i is the local incidence angle, and A_σ is the surface area covered by a pixel. Following Eq. (2.9), two images acquired from different geometries will differ due to the incidence angle dependence of σ^0 and A_σ , even if the observed surface remains unchanged.

Hence, to enable unbiased analysis of SAR images in a GIS and to allow for a joint change detection analysis of SAR amplitude images acquired from different observation geometries, geometric and radiometric distortions in these images need to first be removed. To retrieve the true RCS of the imaged surface σ^0 from

the observed radar data σ , the geometry dependence of σ needs to be removed by correcting for $A_{\sigma}(\theta)$. The process of correcting for $A_{\sigma}(\theta)$ is called Radiometric Terrain Correction (RTC) (Small 2011). RTC includes both geometric terrain correction (geocoding) and radiometric compensation and is typically performed using the following steps:

- Geometric terrain correction (geocoding) is conducted to remove geometric image distortions. A DEM is needed to correct the location of topographically inclined pixels. In areas between $\pm 60^{\circ}$ geographic latitude, the DEM provided by the Shuttle Radar Topography Mission (SRTM) should be sufficient (Gesch et al. 2014).
- Radiometric terrain normalization is performed to remove geometry-dependent radiometric distortions corresponding to a pixel-by-pixel estimation and compensation of $A_{\sigma}(\theta)$ using a DEM. The radiometric normalization technique in Small (2011) is applied.

Figure 2.12 shows an example of the effects of geometric and radiometric normalization. **Figure 2.12(a)** shows an original ALOS PALSAR image over an area near the Denali fault in Alaska. The effects of geometric correction are shown in **Figure 2.12(b)**, and the effects of radiometric normalization are presented in **Figure 2.12(c)**. The normalized data are now largely devoid of geometric influences, reducing radiometric differences between images acquired from different geometries. As a consequence, the RTC-corrected image data show improved performance when combined with other remote sensing datasets and in multi-geometry change detection.

2.6.1.2 More Information on Geocoding and RTC Processing

To learn more about the theory behind geocoding and RTC processing please visit Lecture 9 of UAF's [Online Class on Microwave Remote Sensing](#). You can find Lecture 9 in [Class Module 2 "Imaging Radar Systems."](#) To go directly to the slide deck, [click here](#).

2.6.2 THEORY OF INTERFEROMETRIC SAR

InSAR processing exploits the difference between the phase signals of repeated SAR acquisitions to analyze the shape and deformation of the Earth's

Supplemental materials on InSAR

The Principles and Applications of Interferometric SAR (InSAR):

Interferometric SAR (InSAR) analyzes phase differences between two or more SAR acquisitions with the goal of measuring surface topography and/or surface deformation. While the quality of derived topographic information depends on the relative observation geometry of the SAR acquisitions used, surface deformation can be measured at a fraction of the signal wavelength and, hence, with millimeter to centimeter accuracy. In this lecture, you will hear about the concepts of InSAR and the general processing approaches to arrive at either surface topography or surface deformation. Limitations of InSAR as well as advanced processing concepts will be covered in future lectures.

Link: https://radar.community.uaf.edu/files/2017/03/Lecture12_ConceptsAndGeneralApproachesOfInSAR.pdf

Phase Unwrapping & Limitations of Traditional InSAR Methods:

The first part of this lecture will deal with the problem of phase unwrapping. As InSAR phase measurements are initially only available wrapped into the value range, a phase unwrapping process has to be applied to create an unambiguous phase map ready for topography or deformation analysis. You will be introduced to the general process of phase unwrapping and learn about several popular solutions to this problem. In the second part of this lecture, we will look into the main limitations of the traditional two-image InSAR approach. These identified limitations will set us up for future lectures, which will describe advanced processing techniques (e.g., PS- and SBAS InSAR).

Link: https://radar.community.uaf.edu/files/2017/03/Lecture13_PhaseUnwrappingandLimitationsofInSAR.pdf

The Role of InSAR in Geophysics:

Intrinsically, InSAR is a geodetic discipline, providing accurate measurements of surface deformation. While this is interesting by itself, geoscientists are typically more interested in the geophysical source that causes an observed deformation rather than the deformation itself. Using volcanic activity as an example, this lecture will provide you with some insight on how geophysical parameters can be determined using InSAR measurements in combination with inverse modeling.

Link: https://radar.community.uaf.edu/files/2017/03/Lecture14_UsingInSARinGeophysics.pdf

surface. While the principles and processing flows of InSAR will not be described here in detail, is recommended to look through the following material that is available freely and openly online. The lecture materials listed are part of a full-semester, graduate-level class on microwave remote sensing offered by the University of Alaska Fairbanks, listed in the "Supplemental materials on InSAR" callout.

2.6.2.1 A Word on Sentinel-1 Interferometric Wide Swath Data

The Interferometric Wide (IW) swath mode is the main acquisition mode over land for Sentinel-1. It acquires data with a 250-km swath at 5-x-20-m spatial resolution (single look). Interferometric wide mode

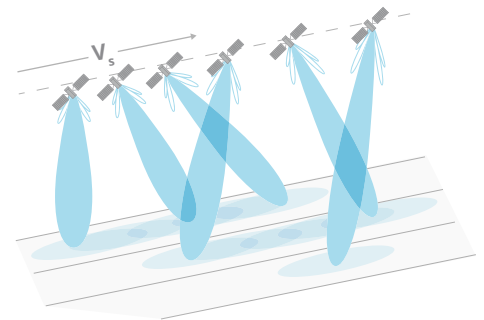


Figure 2.13 TOPSAR acquisition principle.

captures three sub-swaths using the TOPSAR acquisition principle. With the TOPSAR technique, in addition to steering the beam in range as in ScanSAR, the beam is also electronically steered from backward

to forward in the azimuth direction for each burst, avoiding scalloping and resulting in homogeneous image quality throughout the swath. A schematic of the TOPSAR acquisition principle is shown in **Figure 2.13**.

The TOPSAR mode replaces the conventional ScanSAR mode, achieving the same coverage and resolution as ScanSAR, but with nearly uniform image quality (in terms of signal-to-noise ratio and distributed target ambiguity ratio).

Interferometric wide SLC products contain one image per sub-swath and one per polarization channel, for a total of three (single-polarization) or six (dual-polarization) images in an IW product. Each sub-swath image consists of a series of bursts, where each burst has been processed as a separate SLC image. The individually focused complex burst images are included, in azimuth-time order, into a single sub-swath image with black-fill demarcation in between.

2.6.3 CHANGE DETECTION USING SAR

2.6.3.1 Problem Statement

Detecting changes in land-use/land-cover is one of the most fundamental and common uses of remote sensing image analysis. One of the most rudimentary forms of change detection is the visual comparison of two images by a trained interpreter. With an effective display system large enough to display both images simultaneously and to explore and digitize with a cursor tracking to the same location in both images, this is a quick method that can be used to locally collect valuable GIS-compatible data while streaming the images themselves over a relatively low-bandwidth Internet connection.

In an attempt to automate change detection (and hence make it available for large-scale and more operational implementation), a wealth of digital change detection algorithms have been developed over the last decade that operate on a range of different sensors and are grouped into “supervised” and “unsupervised” categories. While a great many methods for detecting changes from remote sensing data are available in literature, this short introduction is limited to methods that are used in reference to SAR.

2.6.3.2 Summary of SAR-Based Change

Detection Techniques

Even when limiting research to SAR-based change detection only, the number of algorithms proposed in recent years can seem overwhelming. Hence, instead of providing an extensive summary of all available techniques, this section attempts to categorize techniques to help in choosing the right method for an envisioned application. Methods will be categorized using several indicators such as by the type of input information needed, the required amount of training data, and the amount of processing expertise needed to implement the algorithms.

2.6.3.2.1 Input Data Used for Change Detection

SAR-based change detection techniques can be categorized by the type of SAR information used for change identification. Categories include “amplitude-based methods,” “phase/coherence-based techniques,” and “polarimetric techniques.”

Amplitude-based methods focus on the RCS information contained in the data, initially ignoring information coming from phase and polarization. One of the advantages of amplitude-based methods lies in their ability maximize the temporal sampling that can be achieved with SAR-based change detection information. Amplitude information is available for every SAR collection, making every new image useful for change detection. As not all SAR acquisitions allow for the use of phase and/or polarization, amplitude data naturally lead to better temporal sampling. This benefit can be further enhanced if RTC is applied to all images. As RTC processing removes most geometry-dependent distortions from the measured SAR RCS, it allows for combining SAR data acquired from multiple incidence angles, leading to further improvements in temporal sampling. However, a disadvantage of amplitude-based methods relates to its limited sensitivity, which often increases the likelihood of false negatives, in which true changes are erroneously missed in the classification.

Phase/coherence-based techniques utilize the fact that significant surface change results in a significant reduction of interferometric coherence, enabling the automatic detection of change via coherence thresholding. Coherence-based techniques are

highly sensitive to change, which interestingly is both the main advantage and disadvantage of this category. On one hand, the high sensitivity is an asset, as it reduces the likelihood for false negatives. On the other, coherent change detection methods tend to have very large false positive rates, where change is vastly overestimated. While methods have been developed to combat these problems, the need for false positive correction makes coherence-based methods appear very complicated and non-straightforward for the uninitiated user. Coherent image pairs are required for these methods to be applicable, which somewhat limits the temporal sampling that can be achieved.

Polarimetric techniques are often highly capable, as they can analyze surface changes across several polarimetric channels. This maximizes the likelihood of change detection and allows one to associate those changes with scattering types (e.g., changes associated with double-bounce, roughness, and volume scattering). The latter is especially relevant, as it enables one to ascertain as to whether a change signature is related to vegetation or the ground, enabling change classification. However, the main disadvantage of polarimetric change detection is related to its reliance on multi-polarization data, which are not always available. Furthermore, polarimetric processing theory may be a bit overwhelming to uninitiated readers.

Independent of change detection methods, the proper choice of sensor is essential to optimizing change detection performance. In particular, the choice of sensor wavelength should be appropriate given the surface and vegetation characteristics of an area of interest. If changes underneath vegetation canopies are the target, longer wavelength sensors are preferred. For bare surfaces, shorter wavelengths often have an advantage. This is because shorter wavelength sensors often increase the RCS associated with rough surfaces and provide more dynamic range that can be used for the identification of change.

2.6.3.2.2 Supervised vs. Unsupervised Methods

Change detection can be performed either unsupervised (Bruzzone & Prieto 2000) or supervised (Huo et al. 2010). In unsupervised change detection,

a change map is generated by comparing objects in two images with a similarity metric. The change map then undergoes thresholding to classify each pixel into changed and unchanged classes (Bruzzone & Prieto 2000, Otsu 1979). In supervised change detection, training samples are selected from the available dataset and are used to train a classifier, which is then used to classify an image into changed and unchanged classes (Huo et al. 2010).

Supervised methods are useful, as radar signatures associated with change do not always have to be theoretically understood to be able to detect them. Instead, the impact of a surface change on the signal observed by a SAR is learned using training data, reducing the need for sophisticated modeling. The reliance on reference data, however, is also the main downside of these methods, as training data are sometimes hard to come by and are seldom free

	AMPLITUDE-BASED	PHASE-BASED	POLARIZATION-BASED
Supervised	White, 1991 Gong et al., 2016 Liu et al., 2016 Gong et al., 2017	Gamba et al., 2007 Pulvirenti et al., 2016	Marino and Hajnsek, 2014
Unsupervised	Meyer et al., 2014 Ajadi et al., 2016 Bruzzone and Prieto, 2000 Bazi et al., 2005 Celik, 2010 Bovolo and Bruzzone, 2005	Yun et al., 2015a Yun et al., 2015b Sharma et al., 2017	Akbari et al., 2016

Table 2.8 List of change detection methods categorized by source data and need for reference data.

of errors. Some recent supervised algorithms based on amplitude, phase, and polarization data are listed in **Table 2.8**.

Unsupervised methods have the advantage that no reference data are required to arrive at a classification result. Instead, signal models are used to encode the impact of surface change on the observed

data. Unsupervised techniques are particularly beneficial in hazard monitoring, where changes are often unanticipated and training data are typically not available in time. Selected recent unsupervised change detection methods are listed in **Table 2.8** as a function of input data type.

SARbian – A free and open SAR Operating System:

SARbian is an easy-to-use, Linux-based SAR processing virtual machine provided by the group behind the EO-College initiative (<https://eo-college.org>) that comes loaded with a wide range of currently-available, free-and-open SAR processing and GIS software tools. The virtual machine is completely pre-installed, ready for use in research, education, or operational applications. No knowledge of installation steps is needed. Hence, SARbian is a convenient resource for researchers and decision-makers that are looking for a hassle-free start with SAR.

SARbian can be downloaded from <https://eo-college.org/sarbian>, and comes with the following list of software tools:

- SAR Processing Tools: ESA S1TBX; ASF MapReady; pyroSAR
- SAR Polarimetry: PolSARPro
- SAR Interferometry: DORIS; SNAPHU (phase unwrapping); PyRAT
- GIS Tools: GDAL; QGIS; GRASS GIS
- Supporting Tools: A number of Python, R, and Octave resources

2.7 References

- Ajadi, O. A., Meyer, F. J., and Webley, P. W., 2016, *Change Detection in Synthetic Aperture Radar Images Using a Multiscale-Driven Approach: Remote Sensing*, v. 8, no. 6, p. 482.
- Akbari, V., Anfinsen, S. N., Doulgeris, A. P., Eltoft, T., Moser, G., and Serpico, S. B., 2016, *Polarimetric SAR Change Detection With the Complex Hotelling–Lawley Trace Statistic: IEEE Transactions on Geoscience and Remote Sensing*, v. 54, no. 7, p. 3953-3966.
- Alemohammad, S. H., Jagdhuber, T., Moghaddam, M., and Entekhabi, D., *Decomposing soil and vegetation contributions in polarimetric L-and P-band SAR observations*, in *Proceedings Geoscience and Remote Sensing Symposium (IGARSS), 2016 IEEE International2016, IEEE*, p. 7553-7556.
- Bamler, R., and Eineder, M., 1996, *ScanSAR processing using standard high precision SAR algorithms: IEEE Transactions on Geoscience and Remote Sensing*, v. 34, no. 1, p. 212-218.
- Bamler, R., and Holzner, J., 2004, *ScanSAR interferometry for RADARSAT-2 and RADARSAT-3: Canadian Journal of Remote Sensing*, v. 30, no. 3, p. 437-447.
- Banqué, X., Lopez-Sanchez, J. M., Monells, D., Ballester, D., Duro, J., and Koudogbo, F., 2016, *Polarimetry-based Land Cover Classification with Sentinel-1 Data: Seminarios*, v. 13, p. 07.
- Bazi, Y., Bruzzone, L., and Melgani, F., 2005, *An unsupervised approach based on the generalized Gaussian model to automatic change detection in multitemporal SAR images: IEEE Transactions on Geoscience and Remote Sensing*, v. 43, no. 4, p. 874-887.
- Belcher, D. P., 2008, *Theoretical Limits on SAR Imposed by the Ionosphere: IET Radar Sonar and Navigation*, v. 2, no. 6, p. 435-448.
- Belcher, D. P., and Rogers, N. C., 2009, *Theory and Simulation of Ionospheric Effects on Synthetic Aperture Radar: IET Radar Sonar and Navigation*, v. 3, no. 5, p. 541-551.
- Bovolo, F., and Bruzzone, L., 2005, *A detail-preserving scale-driven approach to change detection in multitemporal SAR images: IEEE Transactions on Geoscience and Remote Sensing*, v. 43, no. 12, p. 2963-2972.
- Bruniquel, J., and Lopes, A., 1997, *Multi-variate optimal speckle reduction in SAR imagery: International Journal of Remote Sensing*, v. 18, no. 3, p. 603-627.
- Bruzzone, L., and Prieto, D. F., 2000, *Automatic analysis of the difference image for unsupervised change detection: IEEE Transactions on Geoscience and Remote sensing*, v. 38, no. 3, p. 1171-1182.
- Buades, A., Coll, B., and Morel, J. M., *A non-local algorithm for image denoising*, in *Proceedings 2005 IEEE Computer Society Conference on Computer Vision and Pattern Recognition (CVPR'05)20-25 June 2005 2005, Volume 2*, p. 60-65 vol. 62.
- Celik, T., 2010, *A Bayesian approach to unsupervised multiscale change detection in synthetic aperture radar images: Signal Processing*, v. 90, no. 5, p. 1471-1485.
- Chen, S., Hou, J., Zhang, H., and Da, B., 2014, *De-speckling method based on non-local means and coefficient variation of SAR image: Electronics Letters*, v. 50, no. 18, p. 1314-1316.
- Cumming, I. G., and Wong, F. H., 2005, *Digital Processing of Synthetic Aperture Radar Data*, Norwood, MA, Artech House, Inc.
- De Zan, F., and Monti Guarnieri, A., 2006, *TOPSAR: Terrain Observation by Progressive Scans: IEEE Transactions on Geoscience and Remote Sensing*, v. 44, no. 9, p. 2352-2360.
- Di Martino, G., Di Simone, A., Iodice, A., and Riccio, D., 2016, *Scattering-based nonlocal means SAR despeckling: IEEE Transactions on Geoscience and Remote Sensing*, v. 54, no. 6, p. 3574-3588.
- Eineder, M., Adam, N., Bamler, R., Yague-Martinez, N., and Breit, H., 2009, *Spaceborne Spotlight SAR Interferometry With TerraSAR-X: IEEE Transactions on Geoscience and Remote Sensing*, v. 47, no. 5, p. 1524-1535.
- Ferretti, A., Fumagalli, A., Novati, F., Prati, C., Rocca, F., and Rucci, A., 2011, *A New Algorithm for Processing Interferometric Data-Stacks: SqueeSAR: IEEE Transactions on Geoscience and Remote Sensing*, v. 49, no. 9, p. 3460-3470.
- Freeman, A., Krieger, G., Rosen, P., Younis, M., Johnson, W., Huber, S., Jordan, R., and Moreira, A., *SweepSAR: Beam-forming on receive using a reflector-phased array feed combination for spaceborne SAR*, in *Proceedings IEEE Radar Conference, 2009 4-8 May 2009 2009*, p. 1-9.
- Frost, V. S., Stiles, J. A., Shanmugan, K. S., and Holtzman, J. C., 1982, *A model for radar images and its application to adaptive digital filtering of multiplicative noise: IEEE Transactions on Pattern Analysis & Machine Intelligence*, no. 2, p. 157-166.
- Fu, L.-L., and Holt, B., 1982, *Seasat views oceans and sea ice with synthetic-aperture radar*, California Institute of Technology, Jet Propulsion Laboratory.
- Gamba, P., Dell'Acqua, F., and Trianni, G., 2007, *Rapid damage detection in the Bam area using multitemporal SAR and exploiting ancillary data: IEEE Transactions on Geoscience and Remote Sensing*, v. 45, no. 6, p. 1582-1589.
- Gebert, N., Krieger, G., and Moreira, A., 2009, *Digital Beamforming on Receive: Techniques and Optimization Strategies for High-Resolution Wide-Swath SAR Imaging: IEEE Transactions on Aerospace and Electronic Systems*, v. 45, no. 2, p. 564-592.
- Gesch, D. B., Oimoen, M. J., and Evans, G. A., 2014, *Accuracy assessment of the US Geological Survey National Elevation Dataset, and comparison with other large-area elevation datasets: SRTM and ASTER: US Geological Survey*, 2331-1258.
- Gomba, G., Parizzi, A., De Zan, F., Eineder, M., and Bamler, R., 2016, *Toward operational compensation of ionospheric effects in SAR interferograms: the split-spectrum method: IEEE Transactions on Geoscience and Remote Sensing*, v. 54, no. 3, p. 1446-1461.

- Gong, M., Yang, H., and Zhang, P., 2017, *Feature learning and change feature classification based on deep learning for ternary change detection in SAR images: ISPRS Journal of Photogrammetry and Remote Sensing*, v. 129, p. 212-225.
- Gong, M., Zhao, J., Liu, J., Miao, Q., and Jiao, L., 2016, *Change detection in synthetic aperture radar images based on deep neural networks: IEEE transactions on neural networks and learning systems*, v. 27, no. 1, p. 125-138.
- Hooper, B. A., Van Pelt, B., Williams, J., Dugan, J., Yi, M., Piotrowski, C., and Miskey, C., 2015, *Airborne spectral polarimeter for ocean wave research: Journal of Atmospheric and Oceanic Technology*, v. 32, no. 4, p. 805-815.
- Huang, S.-q., Liu, D.-z., Gao, G.-q., and Guo, X.-j., 2009, *A novel method for speckle noise reduction and ship target detection in SAR images: Pattern Recognition*, v. 42, no. 7, p. 1533-1542.
- Huo, C., Zhou, Z., Lu, H., Pan, C., and Chen, K., 2010, *Fast object-level change detection for VHR images: IEEE Geoscience and Remote Sensing Letters*, v. 7, no. 1, p. 118-122.
- Jagdhuber, T., Hajnsek, I., Bronstert, A., and Papathanassiou, K. P., 2013, *Soil moisture estimation under low vegetation cover using a multi-angular polarimetric decomposition: IEEE Transactions on Geoscience and Remote Sensing*, v. 51, no. 4, p. 2201-2215.
- Jehle, M., Frey, O., Small, D., and Meier, E., 2010, *Measurement of Ionospheric TEC in Spaceborne SAR Data: IEEE Transactions on Geoscience and Remote Sensing*, v. 48, no. 6, p. 2460-2468.
- Jehle, M., Ruegg, M., Zuberbuehler, L., Small, D., and Meier, E., 2009, *Measurement of Ionospheric Faraday Rotation in Simulated and Real Spaceborne SAR Data: IEEE Transactions on Geoscience and Remote Sensing*, v. 47, no. 5, p. 1512-1523.
- Kim, J. S., Danklmayer, A., and Papathanassiou, K., *Correction of ionospheric distortions in low frequency interferometric SAR data*, in *Proceedings Geoscience and Remote Sensing Symposium (IGARSS)*, 2011 IEEE International 24-29 July 2011 2011, p. 1505-1508.
- Krieger, G., and Moreira, A., *Potential of digital beamforming in bi- and multistatic SAR*, in *Proceedings Geoscience and Remote Sensing Symposium, 2003. IGARSS '03. Proceedings. 2003 IEEE International 21-25 July 2003 2003*, Volume 1, p. 527-529 vol.521.
- Lanari, R., Tesaura, M., Sansosti, E., and Fornaro, G., 2001, *Spotlight SAR data focusing based on a two-step processing approach: IEEE Transactions on Geoscience and Remote Sensing*, v. 39, no. 9, p. 1993-2004.
- Latini, D., Del Frate, F., and Jones, C. E., 2016, *Multi-frequency and polarimetric quantitative analysis of the Gulf of Mexico oil spill event comparing different SAR systems: Remote Sensing of Environment*, v. 183, p. 26-42.
- Lee, J.-S., 1980, *Digital image enhancement and noise filtering by use of local statistics: IEEE Transactions on Pattern Analysis & Machine Intelligence*, no. 2, p. 165-168.
- Lee, J.-S., Grunes, M., and Mango, S. A., 1991, *Speckle reduction in multipolarization, multifrequency SAR imagery: Geoscience and Remote Sensing, IEEE Transactions on*, v. 29, no. 4, p. 535-544.
- Lee, J.-S., Jurkevich, L., Dewaele, P., Wambacq, P., and Oosterlinck, A., 1994, *Speckle filtering of synthetic aperture radar images: A review: Remote Sensing Reviews*, v. 8, no. 4, p. 313-340.
- Liu, C., Shang, J., Vachon, P. W., and McNairn, H., 2013, *Multiyear crop monitoring using polarimetric RADARSAT-2 data: IEEE Transactions on Geoscience and Remote Sensing*, v. 51, no. 4, p. 2227-2240.
- Liu, R., Jia, Z., Qin, X., Yang, J., and Kasabov, N., 2016, *SAR Image Change Detection Method Based on Pulse-Coupled Neural Network: Journal of the Indian Society of Remote Sensing*, v. 44, no. 3, p. 443-450.
- Lopes, A., Touzi, R., and Nezry, E., 1990, *Adaptive speckle filters and scene heterogeneity: IEEE transactions on Geoscience and Remote Sensing*, v. 28, no. 6, p. 992-1000.
- Lopez-Martinez, C., and Pottier, E., 2007, *On the Extension of Multidimensional Speckle Noise Model from Single-look to Multilook SAR Imagery: IEEE Transactions on Geoscience and Remote Sensing*, v. 45, no. 2, p. 305-320.
- Marino, A., and Hajnsek, I., 2014, *A change detector based on an optimization with polarimetric SAR imagery: IEEE Transactions on Geoscience and Remote Sensing*, v. 52, no. 8, p. 4781-4798.
- Martino, G. D., Simone, A. D., Iodice, A., Riccio, D., and Ruello, G., *Non-local means SAR despeckling based on scattering*, in *Proceedings 2015 IEEE International Geoscience and Remote Sensing Symposium (IGARSS) 26-31 July 2015 2015*, p. 3172-3174.
- Meyer, F., Bamler, R., Jakowski, N., and Fritz, T., 2006, *The Potential of Low-Frequency SAR Systems for Mapping Ionospheric TEC Distributions: IEEE Geoscience and Remote Sensing Letters*, v. 3, no. 4, p. 560-564.
- Meyer, F., and Nicoll, J., *Mapping Ionospheric TEC using Faraday Rotation in Full-Polarimetric L-Band SAR Data*, in *Proceedings European Synthetic Aperture Radar Conference EU-SAR'08, Friedrichshafen, Germany, 2008a*, Volume 2, VDE Verlag, p. 23-26.
- Meyer, F. J., 2011, *Performance Requirements for Ionospheric Correction of Low-Frequency SAR Data: IEEE Transactions on Geoscience and Remote Sensing*, v. 49, no. 10, p. 3694-3702.
- Meyer, F. J., Chotoo, K., Chotoo, S. D., Huxtable, B. D., and Carrano, C. S., 2016, *The Influence of Equatorial Scintillation on L-Band SAR Image Quality and Phase: IEEE Transactions on Geoscience and Remote Sensing*, v. 54, no. 2, p. 869-880.
- Meyer, F. J., McAlpin, D. B., Gong, W., Ajadi, O., Arko, S., Webley, P. W., and Dehn, J., 2014, *Integrating SAR and derived products into operational volcano monitoring and decision support systems: Isprs Journal of Photogrammetry and Remote Sensing*, no. 0.

- Meyer, F. J., and Nicoll, J. B., 2008b, Prediction, Detection, and Correction of Faraday Rotation in Full-Polarimetric L-Band SAR Data: *IEEE Transactions on Geoscience and Remote Sensing*, v. 46, no. 10, p. 3076-3086.
- Migliaccio, M., and Nunziata, F., 2014, On the exploitation of polarimetric SAR data to map damping properties of the Deepwater Horizon oil spill: *International journal of remote sensing*, v. 35, no. 10, p. 3499-3519.
- Mitchard, E. T. A., Saatchi, S. S., Lewis, S. L., Feldpausch, T. R., Woodhouse, I. H., Sonké, B., Rowland, C., and Meir, P., 2011, Measuring biomass changes due to woody encroachment and deforestation/degradation in a forest-savanna boundary region of central Africa using multi-temporal L-band radar backscatter: *Remote Sensing of Environment*, v. 115, no. 11, p. 2861-2873.
- Mittermayer, J., Moreira, A., and Loffeld, O., 1999, Spotlight SAR data processing using the frequency scaling algorithm: *IEEE Transactions on Geoscience and Remote Sensing*, v. 37, no. 5, p. 2198-2214.
- Monti Guarnieri, A., and Prati, C., 1996, ScanSAR focusing and interferometry: *IEEE Transactions on Geoscience and Remote Sensing*, v. 34, no. 4, p. 1029-1038.
- Novak, L. M., and Burl, M. C., 1990, Optimal speckle reduction in polarimetric SAR imagery: *Aerospace and Electronic Systems*, *IEEE Transactions on*, v. 26, no. 2, p. 293-305.
- Otsu, N., 1979, A threshold selection method from gray-level histograms: *IEEE transactions on systems, man, and cybernetics*, v. 9, no. 1, p. 62-66.
- Pi, X., Meyer, F. J., Chotoo, K., Freeman, A., Caton, R. G., and Bridgwood, C. T., Impact of Ionospheric Scintillation on Spaceborne SAR Observations Studied Using GNSS, in *Proceedings ION GNSS2012*, p. 1998-2006.
- Potin, P., Rosich, B., Grimont, P., Miranda, N., Shurmer, I., O'Connell, A., Torres, R., and Krassenburg, M., Sentinel-1 mission status, in *Proceedings EUSAR 2016: 11th European Conference on Synthetic Aperture Radar, Proceedings of 2016, VDE*, p. 1-6.
- Pottier, E., and Lee, J. S., 2009, *Polarimetric Radar Imaging: From Basics to Applications*, Boca Raton, FL, CRC Press; Taylor & Francis Group, 438 p.:
- Pulvirenti, L., Chini, M., Pierdicca, N., and Boni, G., 2016, Use of SAR data for detecting floodwater in urban and agricultural areas: The role of the interferometric coherence: *IEEE Transactions on Geoscience and Remote Sensing*, v. 54, no. 3, p. 1532-1544.
- Quegan, S., Le Toan, T., Skriver, H., Gomez-Dans, J., Gonzalez-Sampedro, M. C., and Hoekman, D. H., Crop classification with multitemporal polarimetric SAR data, in *Proceedings Applications of SAR Polarimetry and Polarimetric Interferometry 2003*, Volume 529.
- Quegan, S., and Yu, J. J., 2001, Filtering of multichannel SAR images: *IEEE Transactions on Geoscience and Remote Sensing*, v. 39, no. 11, p. 2373-2379.
- Sharma, R. C., Tateishi, R., Hara, K., Nguyen, H. T., Gharechelou, S., and Nguyen, L. V., 2017, Earthquake damage visualization (EDV) technique for the rapid detection of earthquake-induced damages using SAR data: *Sensors*, v. 17, no. 2, p. 235.
- Shimada, M., Itoh, T., Motooka, T., Watanabe, M., and Thapa, R., Generation of the first PALSAR-2 global mosaic 2014/2015 and change detection between 2007 and 2015 using the PALSAR and PALSAR-2, in *Proceedings Geoscience and Remote Sensing Symposium (IGARSS), 2016 IEEE International 2016, IEEE*, p. 3871-3872.
- Small, D., 2011, Flattening Gamma: Radiometric Terrain Correction for SAR Imagery: *IEEE Transactions on Geoscience and Remote Sensing*, v. 49, no. 8, p. 3081-3093.
- Sveinsson, J. R., and Benediktsson, J. A., 2003, Almost translation invariant wavelet transformations for speckle reduction of SAR images: *Geoscience and Remote Sensing, IEEE Transactions on*, v. 41, no. 10, p. 2404-2408.
- Van Zyl, J. J., 2011, *Synthetic Aperture Radar Polarimetry*, Hoboken, New Jersey, John Wiley & Sons, Inc, 312 p.:
- Vollmar, F., 1960, Das Telemobiloskop von Christian Hülsmeier, ein früher Vorläufer des Radargeräts: *Deutsches Museum, Abhandlungen und Berichte*, v. 28, p. 33-40.
- Walker, W. S., Stickler, C. M., Kellndorfer, J. M., Kirsch, K. M., and Nepstad, D. C., 2010, Large-area classification and mapping of forest and land cover in the Brazilian Amazon: A comparative analysis of ALOS/PALSAR and Landsat data sources: *Selected Topics in Applied Earth Observations and Remote Sensing, IEEE Journal of*, v. 3, no. 4, p. 594-604.
- Watson-Watt, R., 1946, The evolution of radiolocation: *Journal of the Institution of Electrical Engineers - Part IIIA: Radiolocation*, v. 93, no. 1, p. 11-19.
- White, R., 1991, Change detection in SAR imagery: *International Journal of remote sensing*, v. 12, no. 2, p. 339-360.
- Woodhouse, I. H., 2006, *Introduction to Microwave Remote Sensing*, Boca Raton, FL, CRC Press, Taylor & Francis Group, 400 p.:
- Xie, L., Zhang, H., Wu, F., Wang, C., and Zhang, B., 2015, Capability of rice mapping using hybrid polarimetric SAR data: *IEEE Journal of Selected Topics in Applied Earth Observations and Remote Sensing*, v. 8, no. 8, p. 3812-3822.
- Younis, M., Fischer, C., and Wiesbeck, W., 2003, Digital beamforming in SAR systems: *IEEE Transactions on Geoscience and Remote Sensing*, v. 41, no. 7, p. 1735-1739.
- Yun, S.-H., Fielding, E. J., Webb, F. H., and Simons, M., 2015a, Damage proxy map from interferometric synthetic aperture radar coherence, Google Patents.
- Yun, S.-H., Hudnut, K., Owen, S., Webb, F., Simons, M., Sacco, P., Gurrrola, E., Manipon, G., Liang, C., and Fielding, E., 2015b, Rapid Damage Mapping for the 2015 M 7.8 Gorkha Earthquake Using Synthetic Aperture Radar Data from COSMO-SkyMed and ALOS-2 Satellites: *Seismological Research Letters*, v. 86, no. 6, p. 1549-1556.

DR. FRANZ MEYER'S research focuses on the theory and applications of Synthetic Aperture Radar (SAR) remote sensing data, including the development of SAR processing technology, the analysis of error sources in SAR and InSAR data, and the use of SAR in disaster monitoring. Dr Meyer also works as the Chief Scientist of the Alaska Satellite Facility, NASA's Prime Data Center for SAR data where he is responsible for interactions with the growing SAR user community, the generation of new value added products, and the development of SAR education and training resources. He is a member of the NASA Science team for the US/Indian NISAR satellite and a regular NASA PI for projects focused on SAR research and SAR capacity building.

I want to thank Dr. Olaniyi A Ajadi, Dr. Heming Liao, and Dr. Wenyu Gong (all UAF) for providing input on the development of SAR processing algorithms described in this chapter. All Sentinel-1 SAR data shown above were provided by the Copernicus program and processed by the European Space Agency. All SAR data were accessed through the services of the NASA Alaska Satellite Facility SAR Distributed Active Archive Center (DAAC). I owe gratitude to David B McAlpin (UAF) for proof-reading early drafts of the manuscripts, and to Africa Flores, Kelsey Herndon, and Emil Cherrington (all SERVIR) for their valuable input and editorial support. Finally, I want to thank Bako Mamane (AGRHYMED Regional Centre), Rajesh Thapa (ICIMOD), and all the attendees of our SAR training workshops in Niger and Nepal for their hospitality and for their interest in the rapidly evolving field of radar remote sensing.